

ARMY RESEARCH LABORATORY



Continuum Multiscale Modeling of Finite Deformation Plasticity and Anisotropic Damage in Polycrystals

by J. D. Clayton

ARL-RP-152

September 2006

*A reprint from Theoretical and Applied Fracture Mechanics,
vol. 45, pp. 163–185, 2006.*

NOTICES

Disclaimers

The findings in this report are not to be construed as an official Department of the Army position unless so designated by other authorized documents.

Citation of manufacturer's or trade names does not constitute an official endorsement or approval of the use thereof.

Destroy this report when it is no longer needed. Do not return it to the originator.

Army Research Laboratory

Aberdeen Proving Ground, MD 21005-5066

ARL-RP-152

September 2006

Continuum Multiscale Modeling of Finite Deformation Plasticity and Anisotropic Damage in Polycrystals

J. D. Clayton

Weapons and Materials Research Directorate, ARL

*A reprint from *Theoretical and Applied Fracture Mechanics*,
vol. 45, pp. 163–185, 2006.*

REPORT DOCUMENTATION PAGE			Form Approved OMB No. 0704-0188		
Public reporting burden for this collection of information is estimated to average 1 hour per response, including the time for reviewing instructions, searching existing data sources, gathering and maintaining the data needed, and completing and reviewing the collection information. Send comments regarding this burden estimate or any other aspect of this collection of information, including suggestions for reducing the burden, to Department of Defense, Washington Headquarters Services, Directorate for Information Operations and Reports (0704-0188), 1215 Jefferson Davis Highway, Suite 1204, Arlington, VA 22202-4302. Respondents should be aware that notwithstanding any other provision of law, no person shall be subject to any penalty for failing to comply with a collection of information if it does not display a currently valid OMB control number. PLEASE DO NOT RETURN YOUR FORM TO THE ABOVE ADDRESS.					
1. REPORT DATE (DD-MM-YYYY) September 2006		2. REPORT TYPE Reprint		3. DATES COVERED (From - To) 2003–2006	
4. TITLE AND SUBTITLE Continuum Multiscale Modeling of Finite Deformation Plasticity and Anisotropic Damage in Polycrystals			5a. CONTRACT NUMBER		
			5b. GRANT NUMBER		
			5c. PROGRAM ELEMENT NUMBER		
6. AUTHOR(S) J. D. Clayton			5d. PROJECT NUMBER WHPR01B		
			5e. TASK NUMBER		
			5f. WORK UNIT NUMBER		
7. PERFORMING ORGANIZATION NAME(S) AND ADDRESS(ES) U.S. Army Research Laboratory ATTN: AMSRD-ARL-WM-TD Aberdeen Proving Ground, MD 21005-5066			8. PERFORMING ORGANIZATION REPORT NUMBER ARL-RP-152		
9. SPONSORING/MONITORING AGENCY NAME(S) AND ADDRESS(ES)			10. SPONSOR/MONITOR'S ACRONYM(S)		
			11. SPONSOR/MONITOR'S REPORT NUMBER(S)		
12. DISTRIBUTION/AVAILABILITY STATEMENT Approved for public release; distribution is unlimited.					
13. SUPPLEMENTARY NOTES A reprint from <i>Theoretical and Applied Fracture Mechanics</i> , vol. 45, pp. 163–185, 2006.					
14. ABSTRACT A framework for describing the deformation and failure responses of multi-phase polycrystalline microstructures is developed from micromechanical considerations and volume averaging techniques. Contributions from damage (i.e., displacement discontinuities such as cracks, voids, and shear bands) are captured explicitly in the framework's kinematics and balance relations through additive decompositions of the total deformation gradient and nominal stress, respectively. These additive decompositions—which notably enable description of arbitrarily anisotropic deformations and stresses induced by damage—are derived following the generalized theorem of Gauss, i.e., a version of the divergence theorem of vector calculus. A specific rendition of the general framework is applied to study the response of a dual-phase tungsten (W) alloy consisting of relatively stiff pure W grains embedded in a more ductile metallic binder material. In the present implementation, a Taylor scheme is invoked to average grain responses within each phase, with the local behavior of individual grains modeled with finite deformation crystal plasticity theory. The framework distinguishes between the effects of intergranular damage at grain and phase boundaries and transgranular damage (e.g., cleavage fracture of individual crystals). Strength reduction is induced by the evolving volume fraction of damage (i.e., porosity) and microcrack densities. Model predictions are compared with experimental data and observations for the W alloy subjected to various loading conditions.					
15. SUBJECT TERMS plasticity, fracture, spall, tungsten, damage mechanics					
16. SECURITY CLASSIFICATION OF:			17. LIMITATION OF ABSTRACT UL	18. NUMBER OF PAGES 30	19a. NAME OF RESPONSIBLE PERSON John D. Clayton
a. REPORT UNCLASSIFIED	b. ABSTRACT UNCLASSIFIED	c. THIS PAGE UNCLASSIFIED			19b. TELEPHONE NUMBER (Include area code) 410-306-0975

Continuum multiscale modeling of finite deformation plasticity and anisotropic damage in polycrystals

J.D. Clayton

US Army Research Laboratory, Aberdeen Proving Ground, MD 21005-5069, USA

Available online 4 May 2006

Abstract

A framework for describing the deformation and failure responses of multi-phase polycrystalline microstructures is developed from micromechanical considerations and volume averaging techniques. Contributions from damage (i.e., displacement discontinuities such as cracks, voids, and shear bands) are captured explicitly in the framework's kinematics and balance relations through additive decompositions of the total deformation gradient and nominal stress, respectively. These additive decompositions—which notably enable description of arbitrarily anisotropic deformations and stresses induced by damage—are derived following the generalized theorem of Gauss, i.e., a version of the divergence theorem of vector calculus. A specific rendition of the general framework is applied to study the response of a dual-phase tungsten (W) alloy consisting of relatively stiff pure W grains embedded in a more ductile metallic binder material. In the present implementation, a Taylor scheme is invoked to average grain responses within each phase, with the local behavior of individual grains modeled with finite deformation crystal plasticity theory. The framework distinguishes between the effects of intergranular damage at grain and phase boundaries and transgranular damage (e.g., cleavage fracture of individual crystals). Strength reduction is induced by the evolving volume fraction of damage (i.e., porosity) and microcrack densities. Model predictions are compared with experimental data and observations for the W alloy subjected to various loading conditions.

Published by Elsevier Ltd.

1. Introduction

Constitutive descriptions for deterioration of material strength capacity due to separation or rupture of material have been the focus of numerous investigations within the context of continuum damage mechanics [1]. For ductile polycrystalline metals, scalar damage descriptions measuring porosity and reflecting inelastic volume changes have received a great deal of attention in the literature [2,3]. Concurrently, representations based on effective configurations with reduced material strength have been popularized, including models featuring scalar damage variables [4] or vector- or higher-rank tensor-based damage variables [5,6]. Tensor-based treatments have also been applied to describe degraded composite materials exhibiting a nominally elastic or viscoelastic response [7]. In brittle ceramics, scalar damage variables are frequently implemented [8], although

E-mail address: jdelclayt@comcast.net

more complex methods have been forwarded to account for anisotropic strain rate accommodation due to distributed microcracking [9]. Non-local or gradient-based measures have also been used for modeling damage in ductile [10] and brittle [11] systems. From a multiscale modeling perspective, it was suggested in [12] that a polycrystal plasticity theory can capture the evolution of crystallographic texture in conjunction with a scalar porosity description. Proposed in [13] is a micromechanics-based model accounting for anisotropic inelastic deformation due to grain boundary sliding and migration.

Presently, empirical scalar-based damage descriptions remain the norm in practical numerical simulations of impact and failure [8,14]. For ductile metals, the model in [4] features a damage parameter—the cumulative scalar plastic strain at failure—whose instantaneous value may depend upon the strain rate, temperature, deviatoric stress, and/or hydrostatic pressure. Macroscopic experiments (e.g., tension and torsion tests) are used to determine failure strains and calibrate other material constants entering the model. However, since parameters are chosen primarily upon consideration of macroscopic (stress–strain) data, the connection between these empirical parameters and detailed elements of the microstructure is not often evident. Furthermore, failure properties are generally isotropic in the sense that the evolution of a directionally invariant scalar parameter (e.g., effective plastic strain at failure) dictates fracture.

Even though micromechanics-based treatments characterizing anisotropic damage have been forwarded in the literature (cf. [9]), these models have yet to surpass, in practical or commercial applications, the empirical scalar-based models that typically feature fewer material parameters and require comparatively less effort to implement in a numerical setting. However, in the near future, detailed multiscale models of damage with explicit links between microstructural properties (e.g., grain size distributions, lattice orientations, and grain boundary character) and macroscopic strength degradation are expected to come to the fore in numerical simulations of structures undergoing failure, enabling design of materials for enhanced performance during failure processes [15], e.g., energy absorption in vehicular impact events or ballistic performance of armor and projectiles. Considering the steady improvement regarding computational capabilities developed over the past decade for modeling defects in microstructures, along with experimental capabilities for acquiring material descriptions and associated properties at increasingly fine length scales, multiscale micromechanics-based approaches akin to that forwarded here appear increasingly promising.

Constructed in the present work is a macroscopic description of damage evolution in multi-phase polycrystals via direct averaging of micromechanical solutions. Following [16], the contributions from various damage mechanisms of arbitrary geometry are explicitly accounted for in the deformation gradient decomposition, leading to a precise description of the kinematics of anisotropic damage. While the model is more complex than many of the above-mentioned scalar-based empirical approaches, the connection of material parameters to the microstructure—such as lattice orientation and grain boundary content—is more immediately apparent.

The focus of the model presented here is the thermomechanical behavior of metallic polycrystals. In crystal plasticity theory [17], slip system geometries are tracked explicitly and as a result account for elastic–plastic anisotropy. However, damage evolution on individual crystallographic planes has not been emphasized in the literature for metallic crystals (although the model of Espinosa et al. [9] explicitly accounts for fracture on intrinsically weak planes in ceramic crystals). Failure of preferred lattice planes can dominate the response of certain metallic systems such as body-centered cubic (BCC) tungsten [18]. Furthermore, in multi-phase materials, preferred orientations for strain accommodation due to damage depend upon the grain boundary geometry [19]. Likewise, in materials exhibiting preferred void shapes and arrangements, the contribution to strain anisotropy from damage depends upon the stress state and constraints imposed by the surrounding microstructure.

In Section 2, the general framework, predicated upon explicit volume averaging procedures, is described. Following suggestions in [20,21], the primary mechanical variables upon which the framework is built are the net deformation gradient \mathbf{F} and net nominal stress \mathbf{S} . In Section 3, a particular version of the general framework is developed to study the response of a two-phase tungsten alloy of high interest for use in defense applications. The assumption in [22] will be used to account for the deformation gradient distribution within each phase, with individual grains modeled via crystal plasticity theory. Cleavage fractures are dictated by a traction-based criterion on intrinsically weak crystallographic planes in each W grain [18], while intergranular decohesion is controlled by a stress- and temperature-based model developed following consideration of

previous physical and numerical experiments [19,23–26]. In Section 4, numerical implementation of the framework is described. Model predictions are then discussed in Section 5: the model adequately characterizes the mechanical response of a **W** alloy under tensile loading at low and high strain rates and under shear loading at low strain rates. Conclusions follow in Section 6.

The following notation is used. Vector and tensor quantities are represented with boldface type, while scalars and individual tensor components are written in italics. The index notation is often used, following the Einstein summation convention and distinguishing between covariant (subscript) and contravariant (superscript) components. Juxtaposition implies summation over two repeated adjacent indices (e.g., $(\mathbf{AB})_a^b = A_{ac}B^{cb}$). The dot (scalar) product of vectors is represented by the symbol “ \cdot ” (e.g., $\mathbf{a} \cdot \mathbf{b} = a^a g_{ab} b^b$, with g_{ab} components of the metric tensor). Angled brackets denote a dual (scalar) product (e.g., for second-rank tensors, $\langle \mathbf{A}, \mathbf{B} \rangle = \text{tr}(\mathbf{AB}) = A_{ab}B^{ba}$). The colon denotes contraction over repeated pairs of indices (e.g., $\mathbf{A} : \mathbf{B} = \text{tr}(\mathbf{A}^T \mathbf{B}) = A_{ab}B^{ab}$ and $\mathbf{C} : \mathbf{D} = C^{abcd}D_{cd}$). The symbol “ \otimes ” represents the tensor (outer) product (e.g., $(\mathbf{a} \otimes \mathbf{b})^{ab} = a^a b^b$).

2. Multiscale framework

2.1. Kinematics

Let **X** and **x** denote local fine scale reference and spatial coordinates within a volume element of material. The local deformation gradient **f** is then given by

$$\mathbf{f} \equiv \frac{\partial \mathbf{x}}{\partial \mathbf{X}}, \quad f_{.A}^a \equiv \frac{\partial x^a}{\partial X^A}. \tag{1}$$

The net deformation gradient **F** for the element is then determined from the motion of the volume element’s external boundary:

$$\mathbf{F} \equiv \frac{1}{V} \int_S \mathbf{x} \otimes \mathbf{N} dS, \quad F_{.A}^a \equiv \frac{1}{V} \int_S x^a N_A dS, \tag{2}$$

where **x** in (2) are fine scale spatial coordinates along external surface *S* with outward unit normal **N**. The volume of the material element in the reference configuration is denoted by *V*, and coincident uniform coordinate systems are assumed in each configuration. When the material is damage-free (i.e., the displacement is continuous and differentiable throughout *V*, implying that *V* is simply connected), quantities entering Eqs. (1) and (2) are related by the generalized theorem of Gauss [16,20,21], i.e.,

$$F_{.A}^a \equiv \frac{1}{V} \int_S x^a N_A dS = \frac{1}{V} \int_V \frac{\partial}{\partial X^A} (x^a) dV = \frac{1}{V} \int_V f_{.A}^a dV, \tag{3}$$

meaning that **F** is the exact volume average of **f**. However, when internal surfaces exist within *V*, (3) does not apply. Instead, the volume-averaged deformation gradient $\bar{\mathbf{F}}$ within intact material satisfies

$$\bar{\mathbf{F}} \equiv \frac{1}{V} \int_V \mathbf{f} dV = \frac{1}{V} \int_S \mathbf{x} \otimes \mathbf{N} dS - \frac{1}{V} \int_A \mathbf{x} \otimes \mathbf{N}^d dA, \tag{4}$$

where *A* denotes the union of referential surface areas across which the material displacement becomes discontinuous, with corresponding reference normal \mathbf{N}^d , by convention directed outward from the reference surface into the material. Quantities introduced in Eq. (4) are illustrated in Fig. 1 for the particular case of a polycrystal undergoing intergranular separation, with area *A* consisting of two different grain boundary facets with reference normal vectors $\mathbf{N}_{(1)}^d$ and $\mathbf{N}_{(2)}^d$. Eqs. (2) and (4) may be combined as

$$\mathbf{F} = \frac{1}{V} \int_S \mathbf{x} \otimes \mathbf{N} dS = \underbrace{\frac{1}{V} \int_V \mathbf{f} dV}_{\bar{\mathbf{F}}} + \underbrace{\frac{1}{V} \int_A \mathbf{x} \otimes \mathbf{N}^d dA}_{\mathbf{F}^d} = \bar{\mathbf{F}} + \mathbf{F}^d, \tag{5}$$

emphasizing the additive contributions of bulk material ($\bar{\mathbf{F}}$) and internal surface discontinuities (\mathbf{F}^d) to the net deformation gradient **F** supported by the volume element.

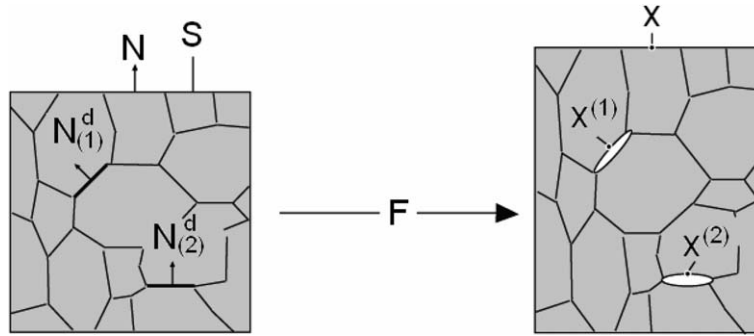


Fig. 1. Finite deformation of polycrystal exhibiting intergranular fracture.

When the geometry of the damage entities may be adequately described via a fewer number of coordinates relative to the geometry of the body, e.g., a planar crack in a three-dimensional body or a shear line discontinuity in a two-dimensional body, Eq. (4) acquires the reduced form [16,19]

$$\bar{\mathbf{F}} \equiv \frac{1}{V} \int_V \mathbf{f} dV = \underbrace{\frac{1}{V} \int_S \mathbf{x} \otimes \mathbf{N} dS}_{\mathbf{F}} - \underbrace{\frac{1}{V} \int_A [[\mathbf{x}]] \otimes \mathbf{N}^d dA}_{\mathbf{F}^d}, \tag{6}$$

where the displacement jump $[[\mathbf{x}]] = \mathbf{x}^+ - \mathbf{x}^-$ and the normal covector $\mathbf{N}^d = \mathbf{N}^{d+} = -\mathbf{N}^{d-}$ on opposing (positive and negative) faces of the discontinuity. Please note that Eqs. (1)–(6) are valid for any solid body, and make no specific assumptions regarding the composition of the material (e.g., crystal structure).

2.2. Stresses and balance relations

Let \mathbf{s} denote the local nominal stress (the transpose of the first Piola–Kirchhoff stress), related to the fine scale Cauchy stress $\boldsymbol{\sigma}$ by $s^{Aa} = j f_b^{-1A} \sigma^{ba}$, where in Cartesian coordinates the Jacobian determinant $j = \det(\mathbf{f})$. The net nominal stress \mathbf{S} for the volume element is defined by

$$\mathbf{S} \equiv \frac{1}{V} \int_S \mathbf{X} \otimes \mathbf{t} dS, \quad S^{Aa} \equiv \frac{1}{V} \int_S X^A t^a dS, \tag{7}$$

where \mathbf{t} is the traction vector per unit reference area acting on external surface S , satisfying $t^a = S^{Aa} N_A$. The conventional local balances of linear and angular momentum are written as

$$\frac{\partial S^{Aa}}{\partial X^A} + b^a = \rho_0 \ddot{x}^a, \quad f_{,A}^a s^{Ab} = f_{,A}^b s^{Aa}, \tag{8}$$

where b^a are components of the body force vector per unit reference volume, and ρ_0 is the reference mass density. When the material element is damage free (simply connected with no internal surface discontinuities), and for the particular case of locally quasi-static conditions and in the absence of local body forces, i.e., $\ddot{x}^a = b^a = 0$, there results [20,21]

$$S^{Aa} = \frac{1}{V} \int_S X^A s^{Ba} N_B dS = \frac{1}{V} \int_V \frac{\partial (X^A s^{Ba})}{\partial X^B} dV = \frac{1}{V} \int_V \left(\frac{\partial s^{Ba}}{\partial X^B} X^A + \delta_B^A s^{Ba} \right) dV = \frac{1}{V} \int_V s^{Aa} dV. \tag{9}$$

However, when the volume element contains internal surfaces with total area A , as well as local inertia and/or body forces, the nominal stress supported by the bulk material $\hat{\mathbf{S}}$ becomes [19]

$$\hat{S}^{Aa} \equiv \frac{1}{V} \int_V \left(\frac{\partial s^{Ba}}{\partial X^B} X^A + \delta_B^A s^{Ba} \right) dV = \underbrace{\frac{1}{V} \int_S X^A t^a dS}_{S^{Aa}} - \underbrace{\frac{1}{V} \int_A X^A (t^d)^a dA}_{(S^d)^{Aa}} = \underbrace{\frac{1}{V} \int_V s^{Aa} dV}_{\bar{S}^{Aa}} + \underbrace{\frac{1}{V} \int_V (\rho_0 \ddot{x}^a - b^a) X^A dV}_{(S^b)^{Aa}} \tag{10}$$

where $\bar{\mathbf{S}}$ is the volume-averaged nominal stress, \mathbf{S}^b is the stress contribution due to micro-inertia and body forces, and \mathbf{S}^d accounts for traction supported by internal surfaces, such that $\mathbf{t} = \mathbf{N}^d \cdot \mathbf{s}$ on local internal surface element dA . Combining Eqs. (7) and (10), the additive nominal stress decomposition is obtained:

$$\mathbf{S} = \bar{\mathbf{S}} + \mathbf{S}^b + \mathbf{S}^d. \tag{11}$$

Analogously to Eq. (6), for a damage entity exhibiting geometry of one spatial dimension less than that of the body, the contribution to the stress from traction on internal surfaces can be written as

$$\mathbf{S}^d = \frac{1}{V} \int_A \mathbf{X} \otimes \llbracket \mathbf{t} \rrbracket dA, \tag{12}$$

where $\mathbf{X} = \mathbf{X}^+ = \mathbf{X}^-$ and the traction jump $\llbracket \mathbf{t} \rrbracket = \mathbf{t}^+ - \mathbf{t}^- = \mathbf{N}^d \cdot (\mathbf{s}^+ - \mathbf{s}^-)$ on opposing (i.e., positive and negative) faces of the internal surface A , for example along opposing sides of a crack front. Notice that \mathbf{S}^d vanishes when all internal surfaces are traction-free. At the macroscopic scale of observation, the stress balance laws are here assumed to exhibit the same form as Eq. (8), i.e.,

$$\frac{\partial S^{Aa}}{\partial X^A} + B^a = \bar{\rho}_0 \ddot{x}^a, \quad F^a_{,A} S^{Ab} = F^b_{,A} S^{Aa}, \tag{13}$$

where \mathbf{X} and \mathbf{x} refer now to macroscopic referential and spatial coordinates, respectively, coincident with their microscopic counterparts, and with $\mathbf{B} \equiv V^{-1} \int_V \mathbf{b} dV$ and $\bar{\rho}_0 \equiv V^{-1} \int_V \rho_0 dV$. Note that Eq. (13) are imposed by assumption and are not direct volume averages of Eq. (8).

2.3. Thermodynamics

The local (fine scale) balance of energy is written as follows:

$$\dot{e} + \text{div}_0 \mathbf{q} - \langle \mathbf{s}, \dot{\mathbf{f}} \rangle = r, \tag{14}$$

with e the internal energy per unit reference volume, \mathbf{q} the heat flux vector per unit reference area, and r the energy source per unit reference volume. Here, div_0 denotes divergence with respect to reference coordinates \mathbf{X} . The local entropy inequality is written as follows, with $\dot{\eta}$ the time rate of entropy production per unit reference volume and θ the local temperature:

$$\dot{\eta} \geq -\text{div}_0 \left(\frac{\mathbf{q}}{\theta} \right) + \frac{r}{\theta}. \tag{15}$$

The Helmholtz free energy per unit reference volume ψ is introduced as

$$\psi \equiv e - \theta \eta, \tag{16}$$

from which, upon substitution of Eqs. (14) and (16) into (15), the entropy relation becomes

$$\langle \mathbf{s}, \dot{\mathbf{f}} \rangle - \frac{\langle \mathbf{q}, \nabla_0 \theta \rangle}{\theta} \geq \dot{\psi} + \dot{\theta} \eta, \tag{17}$$

with ∇_0 the covariant derivative with respect to \mathbf{X} . The local heat flux is dictated by

$$\mathbf{q} = -\mathbf{k} \cdot \nabla_0 \theta, \tag{18}$$

where the contravariant conductivity tensor \mathbf{k} reduces to $k^{AB} = k \delta^{AB}$ for isotropic conduction in a Cartesian reference coordinate system, with δ^{AB} Kronecker's delta.

At the macroscale, relations analogous to Eqs. (14)–(18) are assumed to apply, with $\dot{\mathbf{F}}$ and \mathbf{S} serving as the primary mechanical variables. Define the following quantities:

$$E \equiv V^{-1} \int_V e dV, \quad \bar{\theta} \equiv V^{-1} \int_V \theta dV, \quad R \equiv V^{-1} \int_V r dV. \tag{19}$$

The macrolevel balance of energy is then postulated as

$$\dot{E} + \text{Div}_0 \mathbf{Q} - \langle \mathbf{S}, \dot{\mathbf{F}} \rangle = R, \tag{20}$$

where Div_0 denotes divergence with respect to macroscopic referential coordinates, and where the macroscopic heat flux \mathbf{Q} satisfies

$$\mathbf{Q} = -\mathbf{K} \cdot \bar{\nabla}_0 \bar{\theta}, \quad (21)$$

with $\bar{\nabla}_0$ the macroscopic referential covariant derivative and \mathbf{K} the effective thermal conductivity (note that \mathbf{K} is not necessarily a volume average of \mathbf{k} for heterogeneous microstructures). The macroscopic volumetric free energy is defined by

$$\Psi \equiv E - \bar{\theta} \bar{\eta}, \quad (22)$$

and the reduced entropy equality is introduced at the macro-level:

$$\dot{\bar{\eta}} \geq -Div_0 \left(\frac{\mathbf{Q}}{\bar{\theta}} \right) + \frac{R}{\bar{\theta}}. \quad (23)$$

Here, $\bar{\eta}$ is the macroscopic effective entropy per reference volume for the aggregate, and is not necessarily a volume average. Insertion of Eqs. (20) and (22) into (23) then gives

$$\langle \mathbf{S}, \dot{\mathbf{F}} \rangle - \frac{\langle \mathbf{Q}, \bar{\nabla}_0 \bar{\theta} \rangle}{\bar{\theta}} \geq \dot{\Psi} + \dot{\bar{\theta}} \bar{\eta}, \quad (24)$$

a relationship analogous to fine scale inequality Eq. (17). Please note that Eq. (24) is a strict volume average of Eq. (17) under the following conditions: (i) damage and micro-inertial effects are absent such that $\mathbf{F} = \bar{\mathbf{F}}$ and $\mathbf{S} = \bar{\mathbf{S}}$, (ii) isothermal conditions exist such that temperature rates and temperature gradients vanish, and (iii) particular boundary conditions are applied to the surface S of element V such that the right side of the following equation vanishes [20]:

$$V^{-1} \int_V \dot{\mathbf{f}} \mathbf{s} dV - \dot{\mathbf{F}} \mathbf{S} = V^{-1} \int_S (\dot{\mathbf{x}} - \dot{\mathbf{F}} \mathbf{X}) \otimes \mathbf{n} (\mathbf{s} - \mathbf{S}) dS. \quad (25)$$

Expanding \mathbf{F} and \mathbf{S} via Eqs. (5) and (11), respectively, Eq. (24) becomes

$$\langle \bar{\mathbf{S}} + \mathbf{S}^b + \mathbf{S}^d, \dot{\bar{\mathbf{F}}} \rangle + \langle \bar{\mathbf{S}} + \mathbf{S}^b + \mathbf{S}^d, \dot{\mathbf{F}}^d \rangle - \frac{\langle \mathbf{Q}, \bar{\nabla}_0 \bar{\theta} \rangle}{\bar{\theta}} \geq \dot{\Psi} + \dot{\bar{\theta}} \bar{\eta}. \quad (26)$$

3. Multiscale theory for dual-phase polycrystals

Here the model framework of Section 2 is applied to study cumulative deformation and damage in tungsten alloys. The particular material of interest consists of relatively stiff and brittle pure tungsten grains (BCC) embedded in a relatively compliant and ductile matrix (FCC) consisting of nickel (50 wt.%), iron (25 wt.%), and tungsten (25 wt.%). The composite microstructure nominally is comprised of 90% pure W and 10% matrix alloy, and thus features a net weight distribution of 93W–5Ni–2Fe. Typically, grain sizes span 10–30 μm for the W crystals and 200–500 μm for the FCC phase [19], meaning that multiple W crystals are often embedded within each single crystal of the binder phase. Because of their relatively large mass density, high melting point, and high strength at elevated rates of loading [23–26], tungsten heavy alloys are attractive materials for use in kinetic energy penetrators (i.e., projectiles).

Under high rate impact conditions, tungsten alloys may exhibit a complex set of deformation and damage modes, each describable by the model framework postulated in the present paper. Phenomena of primary interest include:

- Effects of crystallographic texture and grain elongation. In kinetic energy penetrators, swaging and twisting of tungsten rods may produce a preferred orientation of individual W crystals comprising the microstructure. Furthermore, experimental and numerical studies have demonstrated a possible correlation between performance of penetrators and the orientations of crystals comprising their microstructures [27].

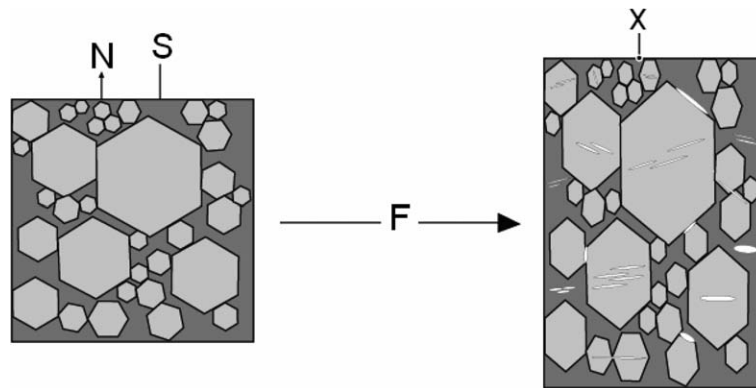


Fig. 2. Finite tensile deformation of dual-phase polycrystalline alloy exhibiting transgranular and intergranular fracture.

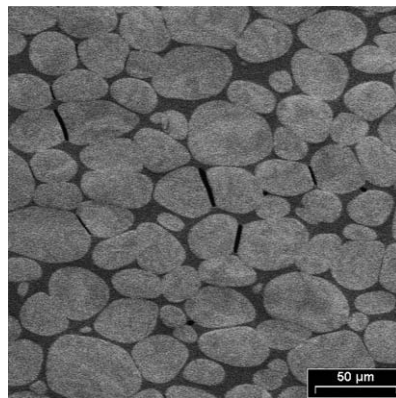


Fig. 3. Intergranular damage at W–W interfaces in 93W–5Ni–2Fe alloy.

- Effects of a variety of fracture mechanisms, as illustrated in Fig. 2. Under positive hydrostatic stress, W alloys are prone to failure by one or more of the following modes [19,25,28]: (i) intergranular fracture at W–W boundaries (Fig. 3), (ii) intergranular fracture at W–binder phase interfaces, (iii) cleavage fracture of W grains, and (iv) intragranular rupture of the binder (i.e., matrix) phase. In penetration applications, tensile stress states often arise when tungsten rods encounter a oblique targets or ricochet, leading to bending and subsequent transverse fracture. Preference of one damage mechanism over the others may depend on processing history, temperature, and loading rate [29].
- Effects of initial microstructure: phase volume fractions and grain boundary contiguity. The volume fraction of binder phase, as well as the connectivity of grain and phase boundaries which act as potential initiation sites for fracture, are known to influence the macroscopic strength and ductility of the alloy [24–26,29].

In what follows, constitutive models for each relevant aspect of tungsten behavior are addressed within the context of the framework of Section 2. Specifically, crystal plasticity models for tungsten and binder phases, intergranular fracture criteria, grain and phase interaction laws, and intergranular failure models are developed, coupled, and merged into our framework.

3.1. Crystal plasticity models for microscopic response

Crystal plasticity models are invoked for the response of each crystal in the dual-phase aggregate. The structure of the model for the tungsten (BCC) and matrix (FCC) phases is similar, though different parameters

are naturally used for each. Only the essential elements are given here; for additional details on model development, the reader is referred to [19].

The local deformation gradient \mathbf{f} of Eq. (1) is decomposed multiplicatively as

$$\mathbf{f} = \mathbf{f}^e \mathbf{f}^\theta \mathbf{f}^p, \tag{27}$$

where \mathbf{f}^e , \mathbf{f}^θ , and \mathbf{f}^p represent, respectively, the kinematics of elasticity and rigid-body rotation, thermal expansion or contraction, and the cumulative contribution of moving crystal defects (i.e., dislocation glide and pseudo-slip due to twinning). The elastic and thermal terms dictate the deformation of the slip direction contravariant vectors $\mathbf{s}^{(\alpha)}$ and slip plane normal covariant vectors $\mathbf{m}^{(\alpha)}$:

$$\mathbf{s}^{(\alpha)} = \mathbf{f}^e \mathbf{f}^\theta \mathbf{s}_0^{(\alpha)}, \quad \mathbf{m}^{(\alpha)} = \mathbf{m}_0^{(\alpha)} \mathbf{f}^{\theta-1} \mathbf{f}^{e-1}. \tag{28}$$

The spatial velocity gradient \mathbf{l} is decomposed as

$$\mathbf{l} \equiv \frac{\partial \dot{\mathbf{x}}}{\partial \mathbf{x}} = \underbrace{\dot{\mathbf{f}} \mathbf{f}^{-1}}_{\equiv \mathbf{l}^e} + \underbrace{\mathbf{f}^e \dot{\mathbf{f}}^\theta \mathbf{f}^{\theta-1} \mathbf{f}^{e-1}}_{\equiv \mathbf{l}^\theta} + \underbrace{\mathbf{f}^e \mathbf{f}^\theta \dot{\mathbf{f}}^p \mathbf{f}^{p-1} \mathbf{f}^{\theta-1} \mathbf{f}^{e-1}}_{\equiv \mathbf{l}^p}, \tag{29}$$

with the superposed dot the material time derivative. Of concern here are cubic lattices. Hence, the thermal deformation is assumed isotropic:

$$\mathbf{l}^\theta = \dot{\mathbf{f}}^\theta \mathbf{f}^{\theta-1} = \alpha_T \dot{\theta} \mathbf{1}, \tag{30}$$

where α_T is the thermal expansion coefficient giving the change in length per unit current length per unit increment in θ , and $\mathbf{1}$ is the unit tensor. The plastic velocity gradient in the intermediate configuration (denoted by $\bar{\mathbf{b}}$ in Fig. 4) is defined as in crystal plasticity theory [17]:

$$\bar{\mathbf{l}}^p \equiv \dot{\mathbf{f}}^p \mathbf{f}^{p-1} = \sum_{\alpha=1}^n \dot{\gamma}^{(\alpha)} \mathbf{s}_0^{(\alpha)} \otimes \mathbf{m}_0^{(\alpha)}, \tag{31}$$

with $\dot{\gamma}^{(\alpha)}$ the plastic shearing rate on slip system α , spanning n total active slip systems.

We assume a Helmholtz free energy potential per unit mass, ϑ , of the form

$$\rho_0^{-1} \psi \equiv \vartheta = \vartheta(\mathbf{e}^e, \theta, \zeta), \tag{32}$$

where the intermediate configuration elastic strain $2(e^e)_{\alpha\beta} = f_{,a}^{ea} g_{ab} f_{,\beta}^{eb} - \tilde{g}_{\alpha\beta}$, with $\tilde{g}_{\alpha\beta}$ a metric tensor on $\tilde{\mathbf{b}}$. The symbol ζ denotes a dimensionless scalar internal variable representing stored micro-elastic energy associated

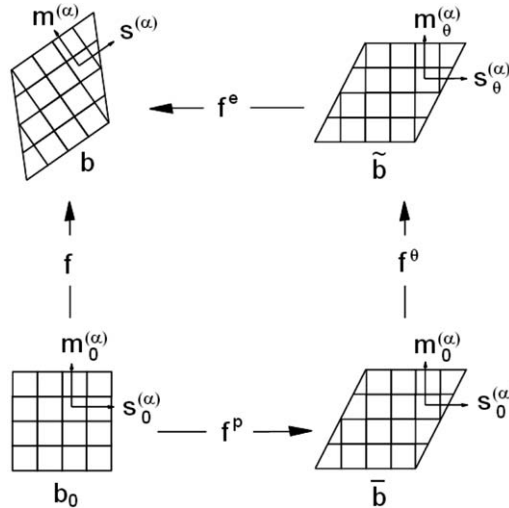


Fig. 4. Deformation maps and configurations of local single crystalline volume element.

with crystal defects that may impede shearing on each slip system (i.e., dislocations). Let $\tilde{\rho}$ denote the mass density in configuration \tilde{b} and let the elastic second Piola–Kirchhoff stress be written $(s^e)^{\alpha\beta} \equiv j^e f_{.a}^{e-1\alpha} \sigma^{ab} f_{.b}^{e-1\beta} = \tilde{\rho} \frac{\partial \vartheta}{\partial e^{\alpha\beta}}$, with $j^e \equiv \tilde{\rho}/\rho$ and $\tilde{\rho}$ the local mass density in configuration \tilde{b} . The resolved Cauchy stress on system α is found by $\tau^{(\alpha)} \equiv \boldsymbol{\sigma} : (\mathbf{g}^{s(\alpha)} \otimes \mathbf{m}^{(\alpha)})$. The localized energy balance in Eq. (14) can be written in the spatial frame as follows [19]:

$$\underbrace{\rho \hat{c} \dot{\theta}}_{\text{temperature change}} = \underbrace{\sum_{\alpha=1}^n \tau^{(\alpha)} \dot{\gamma}^{(\alpha)}}_{\text{plastic dissipation}} - \underbrace{\rho((\partial_{\xi} \vartheta) - \theta(\partial_{\xi} \vartheta)) \dot{\xi}}_{\text{energy of lattice defects}} + \underbrace{\rho \theta \partial_{\theta} e^e \dot{\vartheta} : \dot{\mathbf{e}}^e}_{\text{thermoelastic coupling}} + \underbrace{\text{div}(\mathbf{k} \cdot \nabla_{\mathbf{x}} \theta)}_{\text{heat conduction}} + \underbrace{\frac{\rho}{\rho_0} r}_{\text{heat supply}}. \tag{33}$$

In (33), the specific heat capacity \hat{c} is defined as $\rho_0 \hat{c} \equiv \partial_{\theta} e$. Also, $\nabla_{\mathbf{x}}$ denotes covariant differentiation with respect to fine scale spatial coordinates \mathbf{x} , and div likewise denotes divergence with respect to \mathbf{x} .

When elastic strains are small, the instantaneous response of the material is adequately described by linear hyperelasticity theory. A free energy potential per unit intermediate configuration volume is specified in this case as

$$\tilde{\rho} \vartheta = \frac{1}{2} \mathbf{e}^e : \mathbb{C} : \mathbf{e}^e + \frac{1}{2} \kappa \mu(\theta) \xi^2 + y(\theta), \tag{34}$$

where \mathbb{C} and μ are the fourth rank elastic modulus tensor in configuration \tilde{b} and an effective shear modulus, respectively, and κ is a dimensionless parameter that we assume is independent of strain rate and temperature. The function $y(\theta) = -\hat{c} \theta \ln(\theta/\theta_0)$ accounts for the purely thermal energy, with θ_0 a reference temperature at which $y = 0$. From partial differentiation of (34), we see that the stress satisfies the linear-hyperelastic relationship $\mathbf{s}^e = \mathbb{C} : \mathbf{e}^e$. For an isotropic response, the elastic modulus tensor is given by

$$\mathbb{C}^{\alpha\beta\gamma\delta} = \lambda(\theta) \tilde{g}^{\alpha\beta} \tilde{g}^{\gamma\delta} + \mu(\theta) (\tilde{g}^{\alpha\gamma} \tilde{g}^{\beta\delta} + \tilde{g}^{\alpha\delta} \tilde{g}^{\beta\gamma}), \tag{35}$$

with Lamé’s constant λ and $\tilde{g}^{\alpha\beta}$ contravariant components of the metric tensor on configuration \tilde{b} . Please note that (35) is appropriate as single crystalline tungsten exhibits the unique property of isotropy with respect to elastic constants. Temperature dependencies of moduli of (35) are modeled as follows to first order for pure W:

$$\partial_{\theta} \lambda = C_{1\lambda}^{\theta} + C_{2\lambda}^{\theta} (\theta - 273), \quad \partial_{\theta} \mu = C_{1\mu}^{\theta} + C_{2\mu}^{\theta} (\theta - 273), \tag{36}$$

where $C_{1\lambda}^{\theta}$, $C_{2\lambda}^{\theta}$, $C_{1\mu}^{\theta}$, and $C_{2\mu}^{\theta}$ are material parameters.

A power-law viscoplastic flow rule is invoked to model the time rate of plastic deformation within each crystalline phase of the dual-phase material:

$$\dot{\gamma}^{(\alpha)} = \dot{\gamma}_0 \left(\frac{\tilde{\tau}^{(\alpha)}}{g^{(\alpha)}} \right)^m \text{sgn}(\tilde{\tau}^{(\alpha)}). \tag{37}$$

In (37), $\dot{\gamma}_0$ and m are material constants, $g^{(\alpha)}$ is the slip resistance, $\tilde{\tau}^{(\alpha)} \equiv j^e \tau^{(\alpha)}$, and $\text{sgn}(x) = x/|x|$, with $\text{sgn}(0) = 1$. Thermal softening attributed to increased dislocation mobility at high temperatures is incorporated via the power-law form

$$g^{(\alpha)} = g_0^{(\alpha)} (\theta/\theta_0)^p, \tag{38}$$

with $g_0^{(\alpha)}$ the flow resistance at reference temperature θ_0 and p a dimensionless constant. The following relationship is imposed between the “average” hardening over all systems at fixed reference temperature and the internal variable ξ :

$$\frac{1}{n} \sum_{\alpha=1}^n (g_0^{(\alpha)} - g_y^{(\alpha)}) = \hat{\alpha} \mu \underbrace{b \sqrt{\rho_{\text{T}}}}_{\equiv \xi}, \tag{39}$$

with $g_y^{(\alpha)}$ an initial yield stress, b the magnitude of the Burgers vector, and ρ_{T} the total dislocation line length per unit intermediate configuration volume associated with shearing impedance. The scalar proportionality factor $\hat{\alpha}$ accounts for dislocation interactions. Both lattice friction stress and effects of initial dislocation density are incorporated in the initial yield stress $g_y^{(\alpha)}$.

For the BCC W phase, we allow slip in the $\langle 111 \rangle$ close-packed directions on any of the $\{110\}$ and $\{112\}$ families of planes, meaning the number of potentially active slip systems is $n = 24$. Evolution of slip resistance at reference temperature θ_0 is dictated by a hardening-minus-dynamic-recovery relation:

$$\dot{g}_0^{(x)} = A \sum_{\beta=1}^n q_{\beta}^{\alpha} |\dot{\gamma}^{(\beta)}| - B g_0^{(x)} \sum_{\beta=1}^n |\dot{\gamma}^{(\beta)}|, \quad (40)$$

with the interaction matrix satisfying

$$q_{\beta}^{\alpha} = \delta_{\beta}^{\alpha} + q(1 - \delta_{\beta}^{\alpha}), \quad (41)$$

where q is the latent hardening ratio.

In the W–Ni–Fe matrix material, the number of potentially active slip systems is chosen as $n = 12$. Assume that dislocations glide in $\langle 110 \rangle$ close-packed directions on $\{111\}$ planes for this FCC metal. Elastic isotropy is also assumed for this phase, meaning that Eq. (35) applies, albeit with elastic stiffness constants for the matrix substantially lower in magnitude than those for the pure W. We specify strain rate- and temperature-dependent slip resistances in crystals comprising the more compliant matrix phase via Eqs. (40) and (41), though with different values of A , B , and q than those invoked for the pure W grains.

Material properties for thermoelasticity and plasticity in each phase are listed in Table 1.

3.2. Fracture model for W cleavage

Pure tungsten single crystals are known to fracture along the preferred crystallographic planes having orientations $\{100\}$ and $\{110\}$, with the former characterized by relatively lower fracture toughness than the latter [18]. Furthermore, tungsten exhibits a ductile-to-brittle transition, with cleavage resistance increasing dramatically at ambient temperatures above around 370 K [18,29]. Despite the increase in fracture toughness of W with temperature, O'Donnell and Woodward [29] recorded an increase with temperature in contributions from W cleavage relative to the influence of intergranular fracture and matrix rupture mechanisms in the tensile response of the dual-phase tungsten alloy of primary interest in the present work. The fracture process is thought to commence on weak tungsten-tungsten grain boundaries, and then proceed to subsequent grain

Table 1
Thermoelastic and plastic properties for crystalline phases

Parameter	Value (W)	Value (matrix)
λ	204 GPa	137 GPa
μ	161 GPa	99 GPa
ρ_0	19350 kg/m ³	9200 kg/m ³
\hat{c}	134 J/(kg K)	382 J/(kg K)
$\dot{\gamma}_0$	0.001	0.001
m	20	20
q	1.4	1.0
A	630 MPa	200 MPa
B	1.5	0.4
$g_y^{(x)}$	500 MPa	150 MPa
p	−1.5	−1.5
θ_0	300 K	300 K
α_T	5.3(10) ^{−6} /K	1.5(10) ^{−5} /K
k	160 W/(m K)	100 W/(m K)
$\hat{\alpha}$	0.439	1.03
b	0.275 nm	0.257 nm
κ	1333	200
$C_{1\lambda}^{\theta}$	−3.4 MPa/K	−
$C_{2\lambda}^{\theta}$	0.0065 MPa/K ²	−
$C_{1\mu}^{\theta}$	−10.3 MPa/K	−
$C_{2\mu}^{\theta}$	−0.0041 MPa/K ²	−

cleavage when the number of intergranular fracture sites is insufficient to support crack propagation across the specimen [19,25,28,29].

The present model focuses upon tensile cleavage fracture under mode I conditions. A stress- and temperature-based initiation criterion is proposed, along with a micromechanically inspired model for crack extension on the fracture plane and crack opening normal to the plane of cleavage. Tangential initiation criteria and opening displacements are not considered here, as the material is known to exhibit much greater ductility under shearing and compressive loading conditions [23]. This model accounts for the microstructural configuration on fracture (through the orientation of preferential cleavage planes), and permits anisotropic global deformation due to damage.

The initiation criterion for cleavage fracture is specified as

$$s^{(k)} \equiv s^{Aa} \hat{m}_a^{(k)} \hat{M}_A^{(k)} = \hat{s}^{(k)}(\theta), \tag{42}$$

where s^{Aa} is the local nominal stress, $\hat{m}_a^{(k)}$ and $\hat{M}_A^{(k)}$ are spatial and referential co-vectors normal to potential cleavage planes with index k , and $\hat{s}^{(k)}(\theta)$ is a temperature-dependent fracture strength obeying the linear relationship

$$\hat{s}^{(k)}(\theta) = \begin{cases} C_1^{\{100\}} + C_2^{\{100\}}(\theta - \theta_0) & \text{for } \{100\} \text{ planes,} \\ C_1^{\{110\}} + C_2^{\{110\}}(\theta - \theta_0) & \text{for } \{110\} \text{ planes.} \end{cases} \tag{43}$$

Values of parameters in Eq. (43) were selected upon assuming proportionality between our fracture stress $s^{(k)}$ and the published fracture toughness data of pre-cracked tungsten single crystal bars loaded in three-point bending [18]. Values are listed in Table 2. Upon initiation of damage, i.e., satisfaction of criterion in Eq. (42), crack growth and/or opening may occur on damage plane k . It is assumed here that each grain or sub-grain can support only one microcrack, i.e., fracture is limited to the first plane achieving the criterion in Eq. (42). The contribution of cleavage damage \mathbf{F}_W^d to the global deformation gradient \mathbf{F} is calculated from Eq. (6), where the subscript W corresponds to the pure tungsten phase:

$$\mathbf{F}_W^d = \frac{1}{V} \int_{A_W} [\mathbf{x}] \otimes \mathbf{N}^d dA_W = \frac{f_W}{V_W} \sum_{k=1}^{N_W} ([\mathbf{x}] A_W \otimes \mathbf{N}_W^d)^{(k)} = \frac{f_W}{V_W} \sum_{k=1}^{N_W} (\boldsymbol{\lambda}^d \otimes \hat{\mathbf{M}})^{(k)}. \tag{44}$$

Here summation runs over N_W distinct damage planes, each with corresponding referential area $A_W^{(k)}$. The volume fraction of pure W in the dual-phase system satisfies $f_W = V_W/V$, with $V_W = \sum V_W^{(k)}$ the total volume of the W crystals. For mode I cleavage on preferred planes, the reference orientation satisfies $\mathbf{N}_W^d = \hat{\mathbf{M}}^{(k)}$, and the direction of opening is collinear with $\hat{\mathbf{m}}^{(k)}$, i.e., $\boldsymbol{\lambda}^d = \|\boldsymbol{\lambda}^d\| \hat{\mathbf{m}}^{(k)}$. The magnitude of the crack opening displacement jump (multiplied here by the microcrack area) follows from [9], assuming circular-shaped flaws:

$$\|\boldsymbol{\lambda}^d\| = \begin{cases} \frac{16\pi(1 - \nu^2)}{3E} \left[s^{(k)} \left(r_W^{(k)} \right)^3 \right] \geq 0 & \text{for } s^{(k)} \geq 0, \\ 0 & \text{for } s^{(k)} < 0. \end{cases} \tag{45}$$

Table 2
W grain cleavage properties

$C_1^{\{100\}}$	1.75 GPa
$C_2^{\{100\}}$	0.010 GPa/K
$C_1^{\{110\}}$	1.90 GPa
$C_2^{\{110\}}$	0.010 GPa/K
C_W^R	2.66 km/s
$\dot{\epsilon}_W^0$	$10^4/s$
z_1	1.0
z_2	1.0
r_W^{\max}	30 μm

In Eq. (45), ν and E are Poisson's ratio and Young's modulus for undamaged pure crystalline tungsten, and the crack opening displacement is non-zero only for tensile loading, i.e., for $s^{(k)} > 0$. The microcrack radius and area are related by $A_W^{(k)} = \pi \left(r_W^{(k)} \right)^2$. The time rate of damage deformation is thus dictated by the rate of nominal stress as well as the rate of crack extension, the latter described by a strain rate- and stress-dependent growth law of the form

$$\dot{r}_W^{(k)} = \begin{cases} C_W^R \left(\frac{\dot{\epsilon}}{\dot{\epsilon}_W^0} \right)^{z_1} \left(1 - \frac{\hat{s}^{(k)}}{s^{(k)}} \right)^{z_2} \geq 0 & \text{for } s^{(k)} > \hat{s}^{(k)} \text{ and } r_W^{(k)} < r_W^{\max}, \\ 0 & \text{for } s^{(k)} \leq \hat{s}^{(k)} \text{ or } r_W^{(k)} = r_W^{\max}. \end{cases} \quad (46)$$

Above, C_W^R is the Rayleigh wave speed in pure W, the effective strain rate $\dot{\epsilon} \equiv \sqrt{(2/3)\mathbf{d} : \mathbf{d}}$, with $2d_{ab} = l_{ab} + l_{ba}$, and $\dot{\epsilon}_W^0$ is a normalization parameter required on dimensional grounds. Eq. (46) is a stress- and strain-rate based generalization of the fracture toughness-based approaches of [8,9]. However, in contrast to these approaches, (46) does not require an assumption on the initial crack size in order to propagate damage, such that one may assume $A_W^{(k)}|_{t=0} = 0$ without difficulty. The conditions for crack growth prevent extension when the driving force $s^{(k)} < \hat{s}^{(k)}$ and ensure that the crack diameter does not exceed the physical dimension of grain k , i.e., the grain size r_W^{\max} . Exponents z_1 and z_2 control, respectively, the relative magnitudes of strain rate and stress influences on crack extension. Properties for the cleavage model applied to the particular W heavy alloy considered here are given in Table 2.

The referential orientation unit vector $\hat{\mathbf{M}}^{(k)}$ in Eqs. (42) and (44) remains invariant with time, and depends only upon the initial crystallographic orientation. In contrast, reorientation of the spatial orientation vector follows from

$$\hat{\mathbf{m}}^{(k)} = \mathbf{r}^e \hat{\mathbf{M}}^{(k)}, \quad (47)$$

where \mathbf{r}^e is the elastic rotation of grain k associated with the polar decomposition of the elastic deformation gradient $\mathbf{f}^e = \mathbf{r}^e \mathbf{u}^e$. Thus, under a superposed global rigid body rotation such that $\mathbf{F} \rightarrow \mathbf{Q}\mathbf{F}$, with $\mathbf{Q}^T = \mathbf{Q}^{-1}$ and $\det \mathbf{Q} = 1$, the consistent transformations are $\mathbf{f} \rightarrow \mathbf{Q}\mathbf{f}$, $\mathbf{r}^e \rightarrow \mathbf{Q}\mathbf{r}^e$, and $\mathbf{F}_W^d \rightarrow \mathbf{Q}\mathbf{F}_W^d$.

A strain-like symmetric tensor associated with damage in crystallite k is introduced as

$$\mathbf{C}_W^{\mathbf{d}(k)} \equiv \left(\frac{A_W^{(k)}}{V_W^{(k)}} \|\llbracket \mathbf{x} \rrbracket\| \right)^2 (\mathbf{N}^{\mathbf{d}} \otimes \mathbf{N}^{\mathbf{d}})^{(k)}, \quad (48)$$

the trace of which is found as

$$\text{tr} \left(\mathbf{C}_W^{\mathbf{d}(k)} \right) = \left(\frac{A_W^{(k)}}{V_W^{(k)}} \|\llbracket \mathbf{x} \rrbracket\| \right)^2. \quad (49)$$

Note that for purely mode I fractures, where each corresponding displacement jump and normal vector to the crack plane are co-linear, the volume fraction of damage per unit reference volume of the local grain k is then found, in Cartesian coordinates, by the quantity $\sqrt{\text{tr} \left(\mathbf{C}_W^{\mathbf{d}(k)} \right)}$.

3.3. Intergranular fracture model

The model discussed here collectively accounts for the following three mechanisms of damage in the tungsten alloy: separation at W–matrix interfaces, failure along W–W grain boundaries, and matrix rupture (which is generalized here to include failure at interfaces between two matrix grains as well as crack propagation across matrix grains). The matrix rupture mechanism is labeled here as an intergranular failure mode, as we do not prescribe a damage criterion for cleavage within each individual matrix grain.

Fractures initiate on preferred locations in the microstructure. Experiments have implied that weakest intergranular failure sites in the alloy under consideration are W–W contacts, followed by W–matrix phase boundaries, followed by internal boundaries within the matrix phase [24,25]. However, a previous numerical investigation [19] demonstrated a tendency for initiation on W–W boundaries, even if all interfaces are equally strong, simply due to relatively larger stresses supported by the W grains. Relative strengths of the interfaces

are thought to vary with temperature and processing conditions that may affect impurity concentration at the interfaces [28,29].

Analogously to Eq. (42), stress-controlled damage initiation is assumed. This assertion follows from experimental agreement in peak resolved normal failure stresses observed in macroscopic tension, bending, and spallation [25,28]. Criteria are written in a general form as

$$S^{(i)} \equiv \bar{S}^{Aa} \bar{m}_a^{(i)} \bar{M}_A^{(i)} = \hat{S}^{(i)}(\bar{\theta}), \tag{50}$$

where $\bar{m}_a^{(i)}$ and $\bar{M}_A^{(i)}$ are spatial and referential unit normal vectors to potentially damaged planes, and the index i spans all potential fracture sites for the mechanisms of W–W, W–matrix, and matrix–matrix separation. Components of the total stress S^{Aa} are defined in Eq. (7). Fracture stresses $\hat{S}^{(i)}$ are assumed linearly temperature-dependent and written as

$$\hat{S}^{(i)}(\bar{\theta}) = C_1^I + C_2^I(\bar{\theta} - \theta_0). \tag{51}$$

Here C_1^I and C_2^I are material parameters and $\bar{\theta}$ is the average temperature introduced by definition (19). Note that Eq. (51) assumes normal stress-based initiation; shear stresses are not assumed to initiate damage, following previous arguments and experimental observations. The number, initial orientation $\bar{M}_A^{(i)}$, and maximum size of each potential damage plane must be assigned as initial conditions, based on microstructural characterization. In the implementation that follows, we assume a distribution of damage planes exists encompassing all possible orientations, thereby reducing Eq. (50) to a maximum normal stress criterion with $N_I = 1$. In other words, we assume the existence of a single crack plane of initial orientation $\bar{\mathbf{M}}^{(1)} = \bar{\mathbf{M}}$, where $\bar{\mathbf{M}}$ is the principal direction corresponding to the maximum positive eigenvalue of the symmetric nominal stress tensor $\bar{S}^{Aa} \bar{F}_{.a}^{-1B}$. Furthermore, damage planes are assumed to rotate with the average material deformation $\bar{\mathbf{F}}$ of Eq. (4) in Cartesian coordinates as

$$\bar{\mathbf{m}}^{(i)} = \bar{\mathbf{R}} \bar{\mathbf{M}}^{(i)}, \tag{52}$$

where the polar decomposition of the material deformation is written as $\bar{\mathbf{F}} = \bar{\mathbf{R}} \bar{\mathbf{U}}$.

Upon initiation of damage through attainment of criterion in Eq. (50), crack growth and/or opening may occur on damage plane i . The contribution of damage to the global deformation gradient \mathbf{F} is calculated from Eq. (6), where the subscript label I corresponds to the three aforementioned intergranular mechanisms of interest here:

$$\mathbf{F}_I^d = \frac{1}{V} \int_{A_I} [\mathbf{x}] \otimes \mathbf{N}^d dA_I = \frac{1}{V} \sum_{i=1}^{N_I} ([\mathbf{x}] A_I \otimes \mathbf{N}_I^d)^{(i)} = \frac{1}{V} \sum_{i=1}^{N_I} (\lambda^d \otimes \bar{\mathbf{M}})^{(i)}. \tag{53}$$

Note that A_I spans failure sites along W–W interfaces, W–matrix sites, and matrix internal boundaries, and that for mode I fractures, $\mathbf{N}^{d(i)} = \bar{\mathbf{M}}^{(i)}$ and $\lambda^{d(i)} = \|\lambda^{d(i)}\| \bar{\mathbf{m}}^{(i)}$. From Eqs. (3), (4), (52) and (53), under superposed rigid body rotation, $\mathbf{F} \rightarrow \mathbf{QF}$, $\mathbf{f} \rightarrow \mathbf{Qf}$, and $\bar{\mathbf{F}} \rightarrow \mathbf{Q}\bar{\mathbf{F}}$, leading to the consistent relation $\mathbf{F}_I^d \rightarrow \mathbf{QF}_I^d$.

The magnitude of intergranular crack opening (multiplied here by the crack area, assuming a circular crack of radius $r_1^{(i)}$), is described by a relation analogous to Eq. (45):

$$\|\lambda^{d(i)}\| = \begin{cases} \frac{16\pi(1-\nu^2)}{3E} \left[S^{(i)} \left(r_1^{(i)} \right)^3 \right] \geq 0 & \text{for } S^{(i)} \geq 0, \\ 0 & \text{for } S^{(i)} < 0. \end{cases} \tag{54}$$

Here ν and E are the effective Poisson’s ratio and Young’s modulus for the undamaged dual-phase tungsten alloy, and the crack opening displacement is non-zero only for tensile loading. The microcrack radius and area are related by $A_I^{(i)} = \pi \left(r_1^{(i)} \right)^2$. The rate of crack growth is again described by a stress- and strain rate-driven growth law of the form

$$\dot{r}_1^{(i)} = \begin{cases} C_1^R \left(\frac{\dot{E}}{\dot{E}_0} \right)^{Z_1} \left(1 - \frac{\hat{S}^{(i)}}{S^{(i)}} \right)^{Z_2} \geq 0 & \text{for } S^{(i)} > \hat{S}^{(i)} \text{ and } r_1^{(i)} < r_1^{\max}, \\ 0 & \text{for } S^{(i)} \leq \hat{S}^{(i)} \text{ and } r_1^{(i)} = r_1^{\max}. \end{cases} \tag{55}$$

Table 3
Intergranular fracture properties

C_1^I	1.20 GPa
C_2^I	0.010 GPa/K
C_1^R	2.57 km/s
$\dot{\epsilon}_W^0$	$(2/3)10^4/s$
Z_1	1.0
Z_2	1.0
E	366 GPa
ν	0.29
r_1^{\max}	100 μm

In Eq. (56), C_1^R is the Rayleigh wave speed in the dual-phase alloy (computed from the effective elastic constants of the undamaged composite), the effective strain rate $\dot{\bar{E}} \equiv \sqrt{(2/3)\bar{\mathbf{D}}:\bar{\mathbf{D}}}$, with $2\bar{D}_{ab} = \bar{L}_{ab} + \bar{L}_{ba}$, $\bar{\mathbf{L}} \equiv \bar{\mathbf{F}}\bar{\mathbf{F}}^{-1}$, and $\dot{\epsilon}_W^0$, Z_1 , and Z_2 are material constants analogous to those introduced in Eq. (46). Crack extension is prevented when the driving force $S^{(i)} \leq \hat{S}^{(i)}$, and the crack diameter is forbidden from exceeding the physical dimension r_1^{\max} of oriented surface i . Material parameters for the intergranular damage model are provided in Table 3.

A strain-like symmetric tensor associated with intergranular damage in V , here restricted to a single crack plane ($N_1 = 1$), is introduced as

$$\mathbf{C}_1^d \equiv \left(\frac{A_1}{V} \|\llbracket \mathbf{x} \rrbracket\| \right)^2 (\mathbf{N}^d \otimes \mathbf{N}^d), \quad (56)$$

the trace of which is found as follows, since \mathbf{N}^d is a unit vector:

$$\text{tr}(\mathbf{C}_1^d) = \left(\frac{A_1}{V} \|\llbracket \mathbf{x} \rrbracket\| \right)^2. \quad (57)$$

For purely mode I microcracking, the volume fraction of intergranular damage per unit reference volume of the aggregate is then equal to $\sqrt{\text{tr}(\mathbf{C}_1^d)}$.

3.4. Grain and phase interactions

The general framework introduced thus far allows one to opt for one of a variety of interaction schemes for grains of like and differing phases, for example Taylor [22] or self-consistent schemes [30], or fully resolved calculations at the microscale in which grain and phase topologies are fully described [19]. The latter two methods are accompanied by increased complexity with regards to problem solution (e.g., numerical implementation and computation times). Fully resolved microstructural calculations, in which individual integration points encompass volumes on the scale of a few micrometers, are not yet tractable for solving complex boundary value problems with global dimensions on the order of more than several millimeters.

In the present implementation we employ Taylor's assumption [22] of deformation gradient uniformity among phases comprising each crystalline volume element V . The average material deformation of Eq. (4) is rewritten for the particular alloy of study as

$$\bar{\mathbf{F}} = \underbrace{\frac{f_W}{N_W} \sum_{i=1}^{N_W} \bar{\mathbf{f}}_W^{(i)}}_{\bar{\mathbf{F}}_W} + \underbrace{\frac{f_M}{N_M} \sum_{j=1}^{N_M} \bar{\mathbf{f}}_M^{(j)}}_{\bar{\mathbf{F}}_M}, \quad (58)$$

where subscripts W and M denote grains of pure W phase and matrix binder phase, respectively, N and f represent the number of grains of equal volume and volume fraction of the particular phase, and $\bar{\mathbf{f}}^{(i)}$ ($\bar{\mathbf{f}}^{(j)}$) is the local deformation gradient assumed uniform within grain i (j) of the particular phase. The response of each grain is dictated by the constitutive theory of Section 3.1. The deformation constraint imposed at the phase level is

$$\bar{\mathbf{F}} = f_W^{-1} \bar{\mathbf{F}}_W = f_M^{-1} \bar{\mathbf{F}}_M, \tag{59}$$

and that at the grain scale within each phase is

$$f_W^{-1} \bar{\mathbf{F}}_W = \bar{\mathbf{f}}_W^{(i)}, \quad f_M^{-1} \bar{\mathbf{F}}_M = \bar{\mathbf{f}}_M^{(j)}. \tag{60}$$

Combination of Eqs. (59) and (60) results in a uniform deformation gradient \mathbf{f} for each grain within V , regardless of phase, leading to the well-known upper bound on effective stiffness for the aggregate, in the absence of damage. Previous work [19] has indicated that under high rate tensile loading conditions, the ductile matrix phase tends to accommodate a larger magnitude of strain relative to the stiffer W phase, though at larger deformation levels, assumption Eq. (59) may be more justifiable as strain hardening due to dislocation accumulation leads to a more uniform tangent stiffness among phases [28]. Regardless, Eq. (59) can be used to compare predictions of material response for various microstructural configurations with the caveat that numerical results may be overly stiff.

Average material stresses for the aggregate are found as follows, specialized here to the two-phase tungsten alloy of interest:

$$\bar{\mathbf{S}} = \frac{f_W}{N_W} \sum_{i=1}^{N_W} \bar{\mathbf{s}}_W^{(i)} + \frac{f_M}{N_M} \sum_{j=1}^{N_M} \bar{\mathbf{s}}_M^{(j)}, \tag{61}$$

where $\bar{\mathbf{s}}_W^{(i)}$ and $\bar{\mathbf{s}}_M^{(j)}$ are local nominal stresses in W and matrix phases for each grain i or j . Whereas each grain is assigned the same deformation gradient through Eq. (58), different stresses $\bar{\mathbf{s}}^{(i)}$ arise among grains due to the microstructure (phase and lattice orientation) and corresponding material properties. Note that internal surfaces are presumed traction free, such that the interface-induced stress $\mathbf{S}^d = \mathbf{0}$ in Eqs. (10)–(12). This assumption is thought to be warranted under the mode I fracture modes modeled here, though may not be justified should the model be extended to account for tangential sliding and friction at failed interfaces. As individual grains are not resolved spatially, stresses due to micro-inertia are not computed, i.e., we set $\mathbf{S}^b = \mathbf{0}$ in Eq. (11). In the absence of body forces, this assumption corresponds to uniform acceleration \ddot{x}^a of Eqs. (8) and (10) throughout each grain in V when referred to a local referential coordinate system located at the centroid of each grain. Macro-inertia of Eq. (13) is fully taken into account, however, as the present assumption corresponds to a uniform \ddot{x}^a assigned over each V .

In the present implementation, thermal interactions are neglected between grains and phases, meaning that, depending upon the applied deformation rate, we impose in Eq. (33) either the isothermal constraints $\dot{\theta} = 0$ (low strain rates and long deformation histories) or adiabatic constraints $\langle \mathbf{k}, \nabla_{\mathbf{x}} \theta \rangle = \mathbf{0}$ (high strain rates and short deformation histories), throughout the volume V . This assumption is necessary within the context of the Taylor-type approximations above, as temperature gradients between neighboring grains cannot be spatially resolved.

3.5. Homogenization of damage

Effects from mechanisms modeled individually—elastoplasticity within each phase, cleavage fracture of W grains, and/or intergranular damage modes—are homogenized in a scheme that adheres to the general framework of Section 2. The total deformation gradient for the element V is computed from Eq. (5) as

$$\mathbf{F} = \bar{\mathbf{F}} + \mathbf{F}^d = \bar{\mathbf{F}} + \underbrace{\mathbf{F}_W^d + \mathbf{F}_I^d}_{\mathbf{F}^d}, \tag{62}$$

where $\bar{\mathbf{F}}$ includes the volume-averaged deformation gradients from tungsten and matrix phases, and \mathbf{F}_W^d and \mathbf{F}_I^d are contributions from W cleavage and intergranular mechanisms described by Eqs. (44) and (53), respectively. Total stresses entering Eq. (11) are calculated as follows:

$$\mathbf{S} = \mathbf{A} : \bar{\mathbf{S}}, \quad S^{Aa} = A_{Bb}^{Aa} \bar{S}^{Bb}, \tag{63}$$

where the rank four object \mathbf{A} accounts for stress- and tangent stiffness reduction due to intergranular damage. Note that \mathbf{A} is needed in the present implementation of the model, as strength reduction due to damage is not

accounted for in Eq. (61) or the Taylor-type averaging scheme. However, should the framework be extended to fully resolved calculations at the microscale in which damage entities at grain and phase boundaries are described individually (e.g., [19]), and their effects on the local stress fields within grains are captured explicitly, one may set $\mathbf{\Lambda} = \mathbf{1} \otimes \mathbf{1}$. In the language of continuum damage mechanics [1,5,6], \mathbf{S} of Eq. (63) may be regarded as an ‘effective stress’, and $\mathbf{\Lambda}$ a ‘damage effect tensor’.

As a first approximation, we assume that the average material nominal stress is reduced in an isotropic manner due to microcracking, i.e.,

$$\Lambda_{bb}^{aA} = \Lambda \delta_B^A \delta_b^a, \quad (64)$$

where Λ is a scalar damage variable depending in a multiplicative fashion upon the volume fraction of damage (i.e., porosity), density of cleavage cracks, and density of intergranular cracks:

$$\Lambda = \begin{cases} (1 - \alpha_\varphi \varphi) \left(1 - \alpha_W \frac{\omega_W}{\omega_W^{\max}}\right) \left(1 - \alpha_I \frac{\omega_I}{\omega_I^{\max}}\right) & \text{for } \varphi > 0, \\ 1 & \text{for } \varphi = 0, \\ 0 & \text{for } \varphi \geq \varphi^{\text{fail}}, \omega_I \geq \omega_I^{\text{fail}} \text{ or } \omega_W \geq \omega_W^{\text{fail}}. \end{cases} \quad (65)$$

The fraction of cumulative damage per unit reference volume, φ , is defined by superposition of kinematic quantities introduced in Eqs. (49) and (57):

$$\varphi = \underbrace{\frac{1}{V} \sum_{k=1}^{N_W} V_W^{(k)} \sqrt{\text{tr}(\mathbf{C}_W^{\text{d}(k)})}}_{\text{volume fraction of transgranular damage}} + \underbrace{\sqrt{\text{tr}(\mathbf{C}_I^{\text{d}})}}_{\text{volume fraction of intergranular damage}}. \quad (66)$$

Scalar crack densities are defined in the usual manner as effective cracked areas per unit reference volume:

$$\omega_W \equiv \frac{1}{V} \sum_{k=1}^{N_W} \left(r_W^{(k)}\right)^2, \quad \omega_I \equiv \frac{1}{V} \sum_{i=1}^{N_I} \left(r_I^{(i)}\right)^2. \quad (67)$$

Maximum crack densities supported by each mechanism, denoted by ω_W^{\max} and ω_I^{\max} , are found by substituting respective microstructure parameters r_W^{\max} and r_I^{\max} from Eqs. (46) and (55) into each of Eqs. (67). Critical porosity and crack densities above which total failure (i.e., total stress relief) occurs can be specified in Eq. (65) by parameters φ^{fail} , ω_I^{fail} , and ω_W^{fail} . Relative effects of porosity, crack density on W planes, and crack density at intergranular sites are weighed, respectively, by the scalar material constants α_φ , α_W , and α_I . Note that in the present implementation, strength reduction from damage would not occur under conditions of purely compressive or shear loadings, since only mode I fractures are considered in the fracture models; hence, the specification in Eq. (65) that $\Lambda = 1$ when $\varphi = 0$.

The form of Eq. (65) was postulated in part upon consideration of the following special cases. Setting $\alpha_\varphi = 1$ and $\alpha_W = \alpha_I = 0$ results in $\Lambda = 1 - \varphi$, the usual prescription for the reduction in effective stiffness in an elastic body supporting a dilute concentration of voids (cf. [3]). Setting $\alpha_I = 1$ and $\alpha_\varphi = \alpha_W = 0$ results in $\Lambda = 1 - \omega_I / \omega_I^{\max}$, an appropriate reduction factor for the effective axial stiffness (or stress) of a body containing a single (intergranular) flaw of radius r_I oriented perpendicular to the loading direction [5]. In the present implementation wherein a mixture of damage mechanisms evolves, values of parameters entering (65), listed in Table 4, were chosen such that the model predictions agree with experimental data and observations, as will be discussed more in Section 5.

Table 4
Effective damage properties

α_φ	1.00
α_W	1.00
α_I	0.15
$\omega_W^{\text{fail}} / \omega_W^{\max}$	0.38
$\omega_I^{\text{fail}} / \omega_I^{\max}$	∞
φ^{fail}	∞

Thermodynamic considerations are now revisited briefly for the particular model of Section 3. The macroscopic energy balance Eq. (20) and dissipation inequality (26) become, within the context of constitutive assumptions Eqs. (63) and (64) and adiabatic conditions,

$$\langle A\bar{S}, \dot{\bar{F}} \rangle + \langle A\bar{S}, \dot{\mathbf{F}}_W^d + \dot{\mathbf{F}}_I^d \rangle = \frac{d}{dt} (\Psi + \bar{\theta}\bar{\eta}), \tag{68}$$

$$\langle A\bar{S}, \dot{\bar{F}} \rangle + \langle A\bar{S}, \dot{\mathbf{F}}_W^d + \dot{\mathbf{F}}_I^d \rangle \geq \dot{\Psi} + \dot{\bar{\theta}}\bar{\eta}. \tag{69}$$

4. Numerical implementation

The plasticity and damage model formulated in Section 3 was implemented numerically in order to demonstrate its predictive capabilities and compare these predictions with experimental findings. In the present work the model was implemented within a three-dimensional material point simulator, which could act as a single integration point within a three-dimensional Lagrangian finite element, for example. Deformation-controlled simulations were conducted, with imposed values of $\bar{\mathbf{F}}$ (see Eqs. (58)–(60)) applied to the grains of the microstructure. Thermal conditions were specified as either isothermal or adiabatic.

For numerically integrating the thermomechanical response history of crystals comprising pure W and binder phases according to the constitutive model of Section 3.1, implicit techniques were used, as discussed in detail in [19], and described briefly in what follows. Let subscripts t and $t + \Delta t$ denote consecutive computation instances in a nonlinear analysis, i.e., start and end times in a particular iteration. Inelastic shearing rates for an increment spanning times t and $t + \Delta t$ are found implicitly from values of the resolved shear stress and hardening variables at the end of the iteration:

$$\dot{\gamma}^{(x)} = \dot{\gamma}_0 \left| \frac{\tilde{\tau}_{t+\Delta t}^{(x)}}{g_{t+\Delta t}^{(x)}} \right|^m \text{sgn} \left(\tilde{\tau}_{t+\Delta t}^{(x)} \right). \tag{70}$$

An iterative procedure is invoked to solve Eq. (70), as $\tilde{\tau}_{t+\Delta t}^{(x)}$ and $g_{t+\Delta t}^{(x)}$ depend upon the solution variables $\dot{\gamma}^{(x)}$. For an adiabatic analysis, $\tilde{\tau}_{t+\Delta t}^{(x)}$ and $g_{t+\Delta t}^{(x)}$ depend upon θ , via Eq. (38) and the temperature dependence of elastic moduli. The temperature rate for a given increment spanning t and $t + \Delta t$ is found, from Eq. (33) with $r = 0$, explicitly in terms of quantities at time t :

$$\dot{\theta} = \left(\frac{\beta}{\rho\dot{c}} \sum_{\alpha=1}^n \tau^{(\alpha)} \dot{\gamma}^{(\alpha)} + \frac{\theta}{\dot{c}} \partial_{\theta} (\mathbf{s}^e : \dot{\mathbf{e}}^e) + \frac{1}{\rho\dot{c}} \text{div} (k \nabla_x \theta) \right) \Big|_t, \tag{71}$$

where

$$\beta \equiv \left(\sum_{\alpha=1}^n \tau^{(\alpha)} \dot{\gamma}^{(\alpha)} - \rho ((\partial_{\xi} \vartheta) - \theta (\partial_{\theta \xi} \vartheta)) \dot{\xi} \right) \left(\sum_{\alpha=1}^n \tau^{(\alpha)} \dot{\gamma}^{(\alpha)} \right)^{-1}, \tag{72}$$

meaning that $1 - \beta$ is the ratio of time rates of stored energy to plastic work. The temperature at time $t + \Delta t$ is updated as

$$\theta_{t+\Delta t} = \theta_t + \dot{\theta} \Delta t, \tag{73}$$

and the thermal deformation at the end of the step is determined from

$$\mathbf{f}_{t+\Delta t}^{\theta} = \exp(\alpha_T \dot{\theta} \mathbf{1} \Delta t) \mathbf{f}_t^{\theta}. \tag{74}$$

For each time increment, Eqs. (70) are solved implicitly using values of $\dot{\theta}$, $\theta_{t+\Delta t}$, and $\mathbf{f}_{t+\Delta t}^{\theta}$ found from (71)–(74). The thermoelastic term in Eq. (33) can be rewritten, to first order, as [19]

$$\begin{aligned} \rho \theta \partial_{\theta e^e} \vartheta : \dot{\mathbf{e}}^e &= \theta j^{e-1} \partial_{\theta} (\mathbf{s}^e : \dot{\mathbf{e}}^e) - \rho \theta j^{\theta} \partial_{\theta} (j^{\theta-1}) (\mathbf{s}^e : \dot{\mathbf{e}}^e) \\ &\approx \theta j^{e-1} \{ [(\partial_{\theta} \lambda) \tilde{g}^{\alpha\beta} \tilde{g}^{\gamma\delta} + (\partial_{\theta} \mu) (\tilde{g}^{\alpha\gamma} \tilde{g}^{\beta\delta} + \tilde{g}^{\alpha\delta} \tilde{g}^{\beta\gamma})] (\dot{e}^e)_{\gamma\delta} + 3\alpha_T (j^{\theta-1} s^{e\alpha\beta}) \} (\dot{e}^e)_{\alpha\beta}. \end{aligned} \tag{75}$$

For the pure W grains, possible cleavage fractures are captured by the model features discussed in Section 3.2. In the numerical implementation, prior to the initiation of damage in a particular grain, criterion Eq. (42) is checked at the end of the iteration cycle (i.e., at time $t + \Delta t$) in that grain, for each of the nine potential damage planes ($\{100\}$ and $\{110\}$), with initiation strengths computed via Eq. (43) using updated local temperature values $\theta_{t+\Delta t}$. Upon initiation in a particular crystal, the rate of crack extension for the subsequent time increment, $\dot{r}_W^{(k)}|_{t+\Delta t}$, is computed from Eq. (46), using values of the applied deformation rate imposed (constantly) over the time increment and the projected nominal stress at the end of the increment. In the subsequent cycle, the crack radius is updated simply as

$$r_W^{(k)}|_{t+\Delta t} = r_W^{(k)}|_t + (\Delta t)\dot{r}_W^{(k)}|_{t+\Delta t}, \quad (76)$$

the instantaneous crack opening magnitude is computed from the resolved normal stress from Eq. (45), and the orientation of the crack opening vector in the spatial configuration is updated by the elastic rotation as specified in Eq. (47).

Upon computation of the response (i.e., stress state, temperature, and damage variables) of each crystal of each phase, the average nominal stress $\bar{\mathbf{S}}_{t+\Delta t}$, temperature $\bar{\theta}_{t+\Delta t}$, and intragranular damage deformation $\bar{\mathbf{F}}_W^d|_{t+\Delta t}$ are calculated from respective Eqs. (61), (19) and (44). Then, possible intergranular fractures are addressed by an implementation of the model featured in Section 3.3. Recall that in the present scheme, intergranular fracture is restricted to a single plane whose reference orientation $\bar{\mathbf{M}}$ is determined from a maximum principal stress-based criterion. Before damage develops, the orientation of the potential plane, $\bar{\mathbf{M}}$, is found as the principal eigenvector of the symmetric nominal stress tensor $\bar{\mathbf{S}}^{Aa}\bar{\mathbf{F}}_a^{-1B}|_{t+\Delta t}$. Criterion Eq. (50) is then checked versus the resolved nominal stress due to $\bar{\mathbf{S}}_{t+\Delta t}$, with the initiation strength computed in Eq. (51) using the updated temperature value $\bar{\theta}_{t+\Delta t}$. Upon initiation of intergranular damage, the rate of crack extension for the subsequent time increment, $\dot{r}_I^{(j)}|_{t+\Delta t}$, is computed from Eq. (55), and in the subsequent cycle, the crack radius is updated in a manner analogous to (76). The instantaneous crack opening magnitude is computed from the resolved normal stress using Eq. (53), and the orientation of the crack opening vector in the spatial configuration is updated by the net material rotation as specified by Eq. (52).

At the conclusion of each iteration cycle, the contributions from material deformation, W cleavage, and intergranular fracture are summed using Eq. (62) to yield the total deformation $\mathbf{F}_{t+\Delta t}$. The porosity and microcrack densities are computed via Eqs. (66) and (67), and then substituted into Eq. (65) to compute the damage variable $A_{t+\Delta t}$. Lastly, the effective stress $\mathbf{S}_{t+\Delta t}$ is found from Eq. (63).

Note that the present scheme is easy to implement if numerical crystal plasticity routines are available, as the damage computations are effectively uncoupled from the constitutive update of the elastoplastic response of each crystal. However, we found that very small integration time steps were required to capture the intricacies of damage evolution, due to the explicit time integration of the microcrack radii, Eq. (76). It is understood that should the model be employed in large scale calculations (i.e., a setting with numerous finite elements, for example) the plasticity and damage algorithms may be more efficiently packaged in a fully coupled implicit scheme, though this will require substantial algorithm development due to the unique nature of the kinematic decomposition Eq. (62), and convergence difficulties may arise due to global strain softening in the damaged regime. Furthermore, as the total deformation \mathbf{F} cannot be an outcome in a general large scale simulation, $\bar{\mathbf{F}}$ rather than \mathbf{F} will need to be imposed at each integration point.

5. Results and discussion

Predictions of the model under uniaxial tensile states of stress are discussed first. Deformations and strain rates were prescribed in the simulations according to $\bar{F}^{33} = 1 + \dot{\bar{\epsilon}}t$, with $\dot{\bar{\epsilon}}$ the nominal strain rate in the axial direction (Cartesian coordinates are used here). In the simulations, isothermal conditions ($\theta = 300$ K) were prescribed for low strain rate tests ($\dot{\bar{\epsilon}} = 0.1/s$ and $\dot{\bar{\epsilon}} = 0.0001/s$), and adiabatic conditions were invoked at a higher rate ($\dot{\bar{\epsilon}} = 750/s$), with an initial temperature set to $\theta_0 = 300$ K. As reported in [25], the experimental data were obtained for a 93W–5Ni–2Fe tungsten alloy at low nominal strain rates ($\dot{\bar{\epsilon}} = 0.1/s$ and $\dot{\bar{\epsilon}} = 0.0001/s$) with an Instron test machine, and at the high strain rate ($\dot{\bar{\epsilon}} = 750/s$) with a split Hopkinson

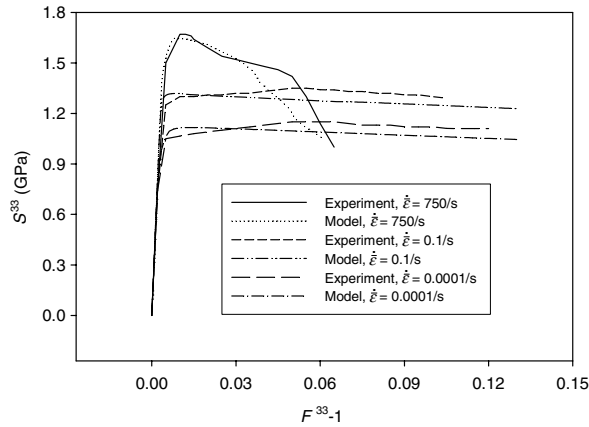


Fig. 5. Tensile stress versus tensile strain.

bar apparatus (i.e., Kolsky bar). The experimental data are representative of behavior observed over numerous tests at each strain rate.

Numerical results from the model are compared with experimental stress–strain data in Fig. 5. In these simulations, random initial lattice orientations were assigned to the polycrystalline aggregate, consisting of 300 W crystals and 100 binder crystals. In the model and in the experiments, peak stresses (i.e., ultimate tensile strengths) increase with increasing applied strain rate, in the former captured by the strain rate sensitivity entering the flow rule Eq. (37). Ductility (i.e., elongation at failure or rupture) tends to decrease with increasing strain rate, as higher tensile stresses more quickly activate a greater number of damage sites (i.e., microfractures) in the material. At the lowest strain rate, $\dot{\epsilon} = 0.0001/s$, the peak average stress S^{33} in the model, 1.12 GPa, is insufficient to activate intergranular damage mechanisms (strength of 1.20 GPa in criterion (50)) or cleavage fracture of any W crystals (strengths of 1.75 GPa and 1.90 GPa for {100} and {110} planes, respectively). At the intermediate strain rate $\dot{\epsilon} = 0.1/s$, intergranular mechanisms are activated but cleavage fractures are not. This prediction (and the assigned material properties in Tables 2 and 3) agrees with experimental observations that intergranular failure modes (most notably W–W boundaries which serve as the weakest link in the microstructure) tend to initiate more readily than cleavage fractures, especially at room temperature [24,25,29]. Finally, at the highest strain rate considered, $\dot{\epsilon} = 750/s$, both inter- and intragranular damage modes are active due to the relatively high tensile stresses, with peak values of S^{33} on the order of 1.65 GPa achieved in both simulation and experiment. At the highest strain rate, total failure of the polycrystalline aggregate was achieved in the simulation when the density of cleavage microcracks reached the limit prescribed in Table 4, $\omega_W^{fail}/\omega_W^{max} = 0.38$, such that the nominal extension at rupture, $F^{33} = 1.06$, matched the experimental result. Notice also in Table 4 that critical values for total rupture via intergranular failure ($\omega_I^{fail}/\omega_I^{max}$) and porosity (ϕ^{fail}) are not assigned, as aforementioned experiments as well as numerical investigations at the microscopic scale [19] have indicated that while evolution of damage typically first occurs at intergranular sites, transgranular fractures must be induced in order to propagate a microcrack across a polycrystalline volume of significant dimensions, to a size large enough to cause catastrophic rupture of the specimen, as not enough intergranular sites exist in the material to exclusively support such a large crack.

Figs. 6(a) and (b) depict the model predictions of crack density and porosity, respectively, at strain rates of $\dot{\epsilon} = 0.1/s$ and $\dot{\epsilon} = 750/s$. Damage initiates early in each case, at an applied stretch around $F^{33} = 1.003$, in reasonable agreement with numerical results of a previous micromechanical investigation [19]. From Fig. 6(a), at the lower strain rate of $\dot{\epsilon} = 0.1/s$, the intergranular crack density (Eq. (67)) saturates to its maximum allowed value at $F^{33} = 1.05$, and cleavage fractures do not occur. On the other hand, at the higher strain rate of $\dot{\epsilon} = 750/s$, both grain boundary and cleavage fractures increase steadily until final rupture occurs at $F^{33} = 1.06$. Similar trends arise for the porosity ϕ in Fig. 6(b): saturation of the volume fraction of intergranular damage occurs at the lower strain rate $\dot{\epsilon} = 0.1/s$, whereas both inter- and intragranular damage contribute steadily to ϕ at the higher rate $\dot{\epsilon} = 750/s$ until rupture. Notice that at the lower strain rate, ϕ decreases

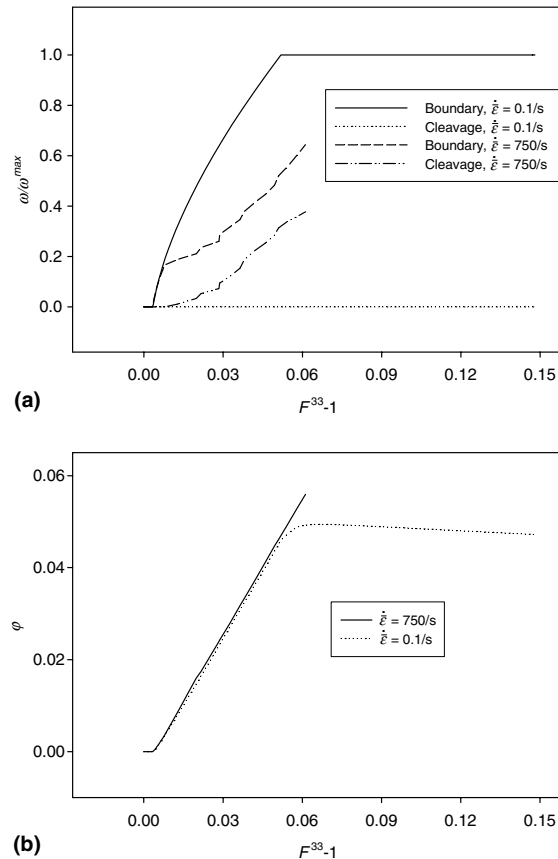


Fig. 6. (a) Normalized damage versus tensile strain and (b) damage versus tensile strain.

very slightly with increasing deformation upon reaching its peak value (on the order of $\varphi = 0.49$), as some elastic microcrack closure takes place due to stress relaxation.

Model results for 60 randomly oriented crystals (50 W grains and 10 binder grains) are compared with results of 400 randomly oriented crystals (300 W grains and 100 binder grains) in Fig. 7. It was found that including more than 400 crystals resulted in negligible changes to the homogenized model predictions for stress-deformation-failure behavior. However, as is clear from Fig. 7, differences in results are apparent when as few as 60 grains are used. In large scale computations, one may choose to include fewer grains (e.g., 60 as opposed to 400) to reduce execution times, should discrepancies on the order of those in Fig. 7 be deemed acceptable.

Effects of various volume fractions of W phase are shown in Fig. 8. As the volume fraction of the stiff W phase increases relative to that of the more ductile binder, the stress S^{33} supported by the aggregate increases at low and high strain rates, in general agreement with experimental trends reported in [26]. However, experimental data [26] also indicate that ductility (i.e., strain at dynamic rupture) should decrease as the volume fraction of W is increased, a phenomenon not captured by the model in Fig. 8, where at the high strain rate, $\dot{\epsilon} = 750/s$, failure occurs consistently at $F^{33} = 1.06$ regardless of volume fraction. A reduction in ductility with increasing volume fraction could easily and logically be captured by allowing critical microcrack densities and porosity listed in Table 4 to depend upon the volume fraction of each phase, though more experimental data is needed to justify for these parameters particular choices of functions of the initial microstructure.

Finally, Fig. 9 compares model predictions with experimental results under torsional (i.e., pure shear) deformation. Deformations and strain rates were prescribed in the simulations according to $\bar{F}^{12} = \dot{\gamma}t$, with $\dot{\gamma}$ the nominal shear strain rate. Isothermal conditions ($\theta = 300$ K) were prescribed for the low strain rate test ($\dot{\gamma} = 0.0001/s$), and adiabatic conditions were invoked at the higher rate ($\dot{\gamma} = 600/s$), with an initial

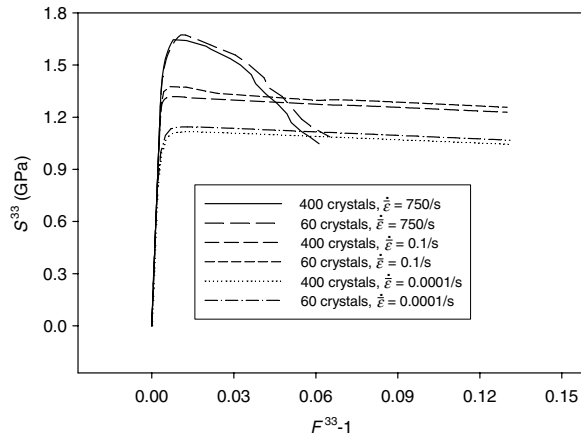


Fig. 7. Tensile stress versus tensile strain.

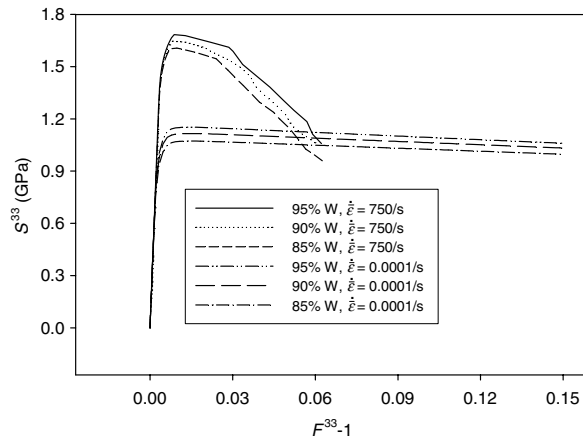


Fig. 8. Tensile stress versus tensile strain.

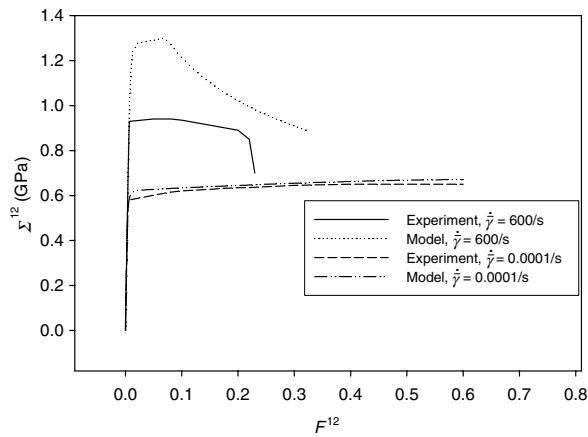


Fig. 9. Shear stress versus shear strain.

temperature of $\theta_0 = 300$ K. Again, 400 randomly oriented grains (300 W and 100 binder) were simulated. The experimental data were obtained for a 93W–5Ni–2Fe tungsten alloy with a split Hopkinson bar apparatus, as discussed in [23]. The macroscopic shear stress Σ^{12} is reported in Fig. 9, where $\Sigma^{ab} = J^{-1} F_{,A}^a S^{Ab}$ is the symmetric Cauchy stress. At the lower strain rate, $\dot{\gamma} = 0.0001/\text{s}$, agreement is excellent between model and experiment, where significant damage does not ensue in either case. At the higher strain rate, $\dot{\gamma} = 600/\text{s}$, the strength predicted by the model is excessive relative to that of the experiment (peak stress of $\Sigma^{12} = 1.30$ GPa versus 0.94 GPa). While mode I damage is captured by the present implementation of the model (and these mechanisms are activated in the simulation at $\dot{\gamma} = 600/\text{s}$), the model does not capture physics of failure reported in the high rate torsion experiments [23]: adiabatic shear localization followed by tangential fracture (modes II and III).

6. Conclusions

Presented, upon invocation of homogenization methods predicated upon the generalized Gauss' theorem, is a multiscale framework for describing finite deformation and failure mechanisms in multi-phase polycrystals. Damage contributions arising from displacement discontinuities such as cracks, voids, and shear bands are captured explicitly in the framework's kinematics and balance relations through additive decompositions of the total deformation gradient (Eqs. (5) and (62)) and nominal stress (Eqs. (11) and (61)). The present approach allows for both strain and rotation accommodation due to damage evolution.

A specific version of the framework has been implemented to describe the thermomechanical response of a two-phase tungsten alloy. The complete implementation consists of single crystal plasticity models capturing thermo-elasto-viscoplasticity in each phase, a cleavage fracture model representing failure of tungsten grains, an intergranular fracture model describing damage evolution at grain and phase boundaries, a polycrystal averaging scheme with Taylor constraints, and a damage homogenization model relating the effective stress to porosity and crack densities. Orientation-dependent damage initiation is specified on preferred cleavage planes, with relative fracture strengths scaled in agreement with reported trends in fracture toughness, and ductile-to-brittle transitions are captured to first order by temperature-dependent initiation criteria. Model predictions for stress-versus-deformation behavior agree with experimental results at low and high tensile strain rates and low shear strain rates. The model is unable to match experimental high rate shear data, as sub-models for shear localization and tangential cracking are not included in the present implementation, and remain to be developed in future studies. Additional areas for model development and improvement, as more experimental data become available for validation, include development of a fully anisotropic damage effect tensor entering Eq. (63), relaxation of the Taylor deformation gradient restriction Eq. (60) to capture intergranular interactions, numerical incorporation of heat conduction, and further exploration of the homogenized thermodynamic framework developed in Eqs. (19)–(24) and Eqs. (68) and (69).

Acknowledgement

This work was supported by the US Army Research Laboratory.

References

- [1] D. Krajcinovic, *Damage Mechanics*, North-Holland, Elsevier, Amsterdam, 1996.
- [2] A.L. Gurson, Continuum theory of ductile rupture by void nucleation and growth: Part 1—yield criteria and flow rules for porous ductile media, *J. Eng. Mater. Sci. Technol.* 99 (1977) 2–15.
- [3] D.J. Bammann, E.C. Aifantis, A damage model for ductile metals, *Nucl. Eng. Des.* 116 (1989) 355–362.
- [4] G.R. Johnson, W.H. Cook, Fracture characteristics of three metals subjected to various strains, strain rates, temperatures, and pressures, *Eng. Fract. Mech.* 21 (1985) 31–48.
- [5] S. Murakami, Notion of continuum damage mechanics and its application to anisotropic creep damage theory, *J. Eng. Mater. Technol.* 105 (1983) 99–105.
- [6] A. Menzel, P. Steinmann, Geometrically non-linear anisotropic inelasticity based on fictitious configurations: application to the coupling of continuum damage and multiplicative elasto-plasticity, *Int. J. Numer. Methods Eng.* 56 (2003) 2233–2266.
- [7] R.S. Kumar, R. Talreja, A continuum damage model for linear viscoelastic materials, *Mech. Mater.* 35 (2003) 463–480.

- [8] A.M. Rajendran, D.J. Grove, Modeling the shock response of silicon carbide, boron carbide and titanium diboride, *Int. J. Impact Eng.* 18 (1996) 611–631.
- [9] H.D. Espinosa, P.D. Zavattieri, S.K. Dwivedi, A finite deformation continuum discrete model for the description of fragmentation and damage in brittle materials, *J. Mech. Phys. Solids* 46 (1998) 1909–1942.
- [10] G.Z. Voyiadjis, R.K. Abu Al-Rub, A.N. Palazotto, Thermodynamic framework for coupling of non-local viscoplasticity and non-local anisotropic viscodamage for dynamic localization problems using gradient theory, *Int. J. Plasticity* 20 (2004) 981–1038.
- [11] T.E. Lacy, D.L. McDowell, R. Talreja, Gradient concepts for evolution of damage, *Mech. Mater.* 31 (1999) 831–860.
- [12] S. Ahzi, S. Schoenfeld, Mechanics of porous polycrystals: a fully anisotropic flow potential, *Int. J. Plasticity* 14 (1998) 829–839.
- [13] A. Zubelewicz, Micromechanical study of ductile polycrystalline metals, *J. Mech. Phys. Solids* 41 (1993) 1711–1722.
- [14] H.W. Meyer, D.S. Kleponis, Modeling the high strain rate behavior of titanium undergoing ballistic impact and penetration, *Int. J. Impact Eng.* 26 (2001) 509–521.
- [15] T. Watanabe, Grain boundary design for the control of intergranular fracture, *Mater. Sci. Forum* 46 (1989) 25–48.
- [16] J.D. Clayton, D.L. McDowell, Finite polycrystalline elastoplasticity and damage: multiscale kinematics, *Int. J. Solids Struct.* 40 (2003) 5669–5688.
- [17] C. Teodosiu, F. Sidoroff, A finite theory of elastoplasticity of single crystals, *Int. J. Eng. Sci.* 14 (1976) 713–723.
- [18] P. Gumbsch, J. Riedle, A. Hartmaier, H.F. Fischmeister, Controlling factors for the brittle-to-ductile transition in tungsten single crystals, *Science* 282 (1998) 1293–1295.
- [19] J.D. Clayton, Dynamic plasticity and fracture in high density polycrystals: constitutive modeling and numerical simulation, *J. Mech. Phys. Solids* 53 (2005) 261–301.
- [20] R. Hill, On constitutive macro-variables for heterogeneous solids at finite strain, *Proc. R. Soc. Lond.* A326 (1972) 131–147.
- [21] S. Nemat-Nasser, Averaging theorems in finite deformation plasticity, *Mech. Mater.* 31 (1999) 493–523.
- [22] G.I. Taylor, Plastic strain in metals, *J. Inst. Metals* 62 (1938) 307.
- [23] T. Weerasooriya, P.A. Beaulieu, Effects of strain rate on the deformation and failure behavior of 93W–5Ni–2Fe under shear loading, *Mater. Sci. Eng. A* 172 (1993) 71–78.
- [24] T. Weerasooriya, P. Moy, R. Dowding, Effect of W–W contiguity on the high shear strain rate behavior of 93W–5Ni–2Fe tungsten heavy alloy, in: A. Bose, R. Dowding (Eds.), *Proceedings of the 2nd International Conference on Tungsten and Refractory Metals*, Metal Powder Industries, 1994, pp. 401–409.
- [25] T. Weerasooriya, Deformation and failure behavior of a tungsten heavy alloy under tensile loading at different strain rates, in: *Proceedings of the SEM Annual Conference on Experimental Mechanics*, Charlotte, NC, USA, 2–4 June 2003.
- [26] T. Weerasooriya, P. Moy, High shear strain rate behavior of W–Ni–Fe tungsten heavy alloy composites as a function of matrix volume fraction, *ARL-TR-1964*, 1998.
- [27] S.E. Schoenfeld, D.J. Benson, Modeling penetration mechanisms and ballistic performance in high aspect ratio tungsten single-crystal rods: a crystal plasticity model suitable for impact calculations, in: S.N. Atluri, G. Yagawa (Eds.), *Advances in Computational Engineering Science*, Tech Science Press, 1997, pp. 1116–1121.
- [28] Z. Baoping, Y. Chao, X. Yingming, J. Chunlan, Responsive behaviour of 93 wt.% tungsten alloy under the intense shock loading, in: Z. Zhemin, T. Quingming (Eds.), *Proceedings of IUTAM Symposium on Impact Dynamics*, Peking University Press, Peking, PRC, 1994, pp. 283–297.
- [29] R.G. O'Donnell, R.L. Woodward, Influence of temperature on the fracture of a W–Ni–Fe alloy, *J. Mater. Sci.* 35 (2000) 4319–4324.
- [30] A. Molinari, G.R. Canova, S. Ahzi, A self-consistent approach of the large deformation polycrystal plasticity, *Acta Metall.* 35 (1987) 2983–2994.

NO. OF
COPIES ORGANIZATION

1 DEFENSE TECHNICAL
(PDF INFORMATION CTR
ONLY) DTIC OCA
8725 JOHN J KINGMAN RD
STE 0944
FORT BELVOIR VA 22060-6218

1 US ARMY RSRCH DEV &
ENGRG CMD
SYSTEMS OF SYSTEMS
INTEGRATION
AMSRD SS T
6000 6TH ST STE 100
FORT BELVOIR VA 22060-5608

1 DIRECTOR
US ARMY RESEARCH LAB
IMNE ALC IMS
2800 POWDER MILL RD
ADELPHI MD 20783-1197

3 DIRECTOR
US ARMY RESEARCH LAB
AMSRD ARL CI OK TL
2800 POWDER MILL RD
ADELPHI MD 20783-1197

ABERDEEN PROVING GROUND

1 DIR USARL
AMSRD ARL CI OK TP (BLDG 4600)

NO. OF
COPIES ORGANIZATION

ABERDEEN PROVING GROUND

32 DIR USARL
AMSRD ARL CI HC
P CHUNG
AMSRD ARL WM
J MCCAULEY
T WRIGHT
AMSRD ARL WM MA
W NOTHWANG
AMSRD ARL WM TA
S SCHOENFELD
AMSRD ARL WM TC
M FERMEN COKER
R COATES
AMSRD ARL WM TD
S BILYK
T BJERKE
D CASEM
J CLAYTON (5 CPS)
T CLINE
D DANDEKAR
W EDMANSON
M GREENFIELD
C GUNNARSSON
Y HUANG
K IYER
R KRAFT
B LOVE
S MCNEILL
H MEYER
R MUDD
M RAFTENBERG
E RAPACKI
M SCHEIDLER
S SEGLETES
T WEERASOORIYA

INTENTIONALLY LEFT BLANK.